International Journal of Solids and Structures 256 (2022) 111943

Contents lists available at ScienceDirect

International Journal of Solids and Structures

journal homepage: www.elsevier.com/locate/ijsolstr

X-ray computed tomography analysis of pore deformation in IN718 made with directed energy deposition via in-situ tensile testing

Orion L. Kafka [a,b,*], Cheng Yu [a], Puikei Cheng [a], Sarah J. Wolff [a], Jennifer L. Bennett [a], Edward J. Garboczi [b], Jian Cao [a], Xianghui Xiao [c], Wing Kam Liu [a]

[a] Department of Mechanical Engineering, Northwestern University, United States
[b] National Institute of Standards and Technology, Material Measurement Laboratory, Applied Chemicals and Materials Division, United States
[c] National Synchrotron Light Source II, Brookhaven National Laboratory, United States

ARTICLE INFO

Keywords:
Additive manufacturing
Directed energy deposition
Tensile testing
Mechanical property variations
In-situ X-ray CT
Pore mechanics
Model verification

ABSTRACT

Directed energy deposition (DED) is a metal additive manufacturing technique often used for larger-scale components and part repair. It can result in material performance that differs from conventionally processed metal. This work studies spatial and orientation-based differences in tensile properties of nickel-based alloy IN718 using *in-situ* x-ray computed tomography to observe internal pore populations. Anisotropy and spatial variability in mechanical properties are shown while the evolution of pore shape during deformation is measured. Measured pore deformation is compared to predict deformations simulated using a computational crystal plasticity scheme, which provides insight, through inverse modeling, to the grain orientation in which the pore resides. The measurements provide a high fidelity method to compare experimental and computational approaches to pore deformation studies. Pore deformation measurements show that pores tend to grow and elongate in the direction of loading, consistent with ductile deformation and likely deforming with the material. Generally, the pore defects observed in this material (not from lack-of-fusion) do not cause so-called premature failure, and fully developed necking occurs prior to fracture.

1. Introduction

Many metal additive manufacturing (AM) technologies exist, and each has different material impacts and associated challenges. The work presented here relates specifically to the directed energy deposition (DED) AM technique, where powder is delivered with a shielding gas to a molten pool created by a laser. This can offer more flexibility than powder-bed type AM, with applications such as repair and large area manufacturing possible as described by Shamsaei et al. (2015) and Zhai et al. (2019). The cooling rate typical in DED is between that experienced by conventional casting and powder-bed AM material, meaning that a unique set of microstructures can occur. A variety of other differences in length and time scales mean that the performance of DED-built material is not necessarily similar to cast, wrought, or powder-bed AM processed material, c.f. Sochalski-Kolbus et al. (2015), Schneider (2020), Xavier et al. (2020) and Gordon et al. (2019). Thus, a body of literature related specifically to DED-type processes, and the different alloys used in these processes, needs to be developed to enable confident use of DED materials in structural and high performance applications, such as in structural, aeronautical components (Gorelik, 2017).

This paper first presents an experimental study that focuses on observational and quantitative measurement of the deformation of pores in DED-built nickel-based super-alloy IN718, and pairs this with a computational crystal plasticity analysis of the pore deformation process. IN718 is a commonly used alloy in AM applications, and is relatively easy to process with a laser, because it is precipitation-hardened and quench-suppressible, meaning that it can be deposited and possibly finish-machined in a more malleable state and later heat treated to achieve full strength. This Ni–Fe alloy is used in applications such as gas turbines, space craft, and nuclear reactors because it has high strength, fatigue strength, and corrosion resistance, as well as high creep-rupture strength at elevated temperatures (Zhai et al., 2019).

Previous studies have identified significant anisotropy and variability in as-built, stress-relieved, and heat treated DED IN718, as well as sub-standard material performance, as shown in Liu et al. (2011a), Li et al. (2020), Zhang et al. (2020) and Glerum et al. (2021). Reports have, however, varied with some authors finding wrought-equivalent

* Corresponding author at: National Institute of Standards and Technology, Material Measurement Laboratory, Applied Chemicals and Materials Division, United States.
E-mail addresses: olkafka@u.northwestern.edu, orion.kafka@nist.gov (O.L. Kafka).

https://doi.org/10.1016/j.ijsolstr.2022.111943
Received 5 May 2022; Received in revised form 25 July 2022; Accepted 23 August 2022
Available online 28 August 2022
0020-7683/Published by Elsevier Ltd.

properties particularly after heat treatment (Qi et al., 2009; Lambarri et al., 2013). It has been known for perhaps 10 years that the microstructures and mechanical properties of IN718 depend on many factors in the DED process, including feedstock, process parameters, scan strategy, build conditions, and post-build treatments (Liu et al., 2011a; Blackwell, 2005; Liu et al., 2011b; Parimi et al., 2012). Process monitoring, real-time control, secondary processes, heat treatments, and other techniques can be used to mitigate the worst difficulties with the method, and efforts have been made to in this direction. However, processing defects and particularly microscale pores and undesirable phases can still occur (Bennett et al., 2017; Wolff et al., 2019; Gan et al., 2019; Sui et al., 2019; Jinoop et al., 2019; Ning et al., 2018; Qi et al., 2009; Zhong et al., 2016; Yuan et al., 2018; Zhao et al., 2008). Indeed, several parallel studies to the current work by the same team have recently appeared, focusing on techniques to avoid these factors and specifically employing tests on thin wall specimens similar to those described below, though with a focus on the thermal processing and microstructural aspects rather than the present focus on pores and their deformation mechanisms (Glerum et al., 2021; Bennett et al., 2021).

Mechanical testing with *in-situ* inspection has been used in prior works to assess how microstructures deform during loading, and in particular how the unique features generated by AM processing impact performance. For example, Carlton et al. studied deformation of 316L Stainless Steel with a range of pore defect sizes, concluding that, for relatively dense material, conventional failure processes dominate while for specimens with large pores (the largest was 1100.0×10^4 μm^3) a defect-driven mode would dominate (Carlton et al., 2016). Similarly, Voisin et al. used *in-situ* x-ray diffraction and post-mortem XCT to study the deformation mechanics of AM Ti-6Al-4V, and the impact that even a small volume faction of pores (i.e. $\ll 1$ vol%) has on total strain to failure (Voisin et al., 2018). Kim et al. used lab-scale XCT to measure the evolution of artificially created internal defects in AM 17-4 Stainless Steel, and showed quantitatively that pore growth drives increasing stress concentrations that ultimately result in failure (Kim et al., 2020). More broadly XCT is an important inspection tool that can be useful for discriminating between dangerous and harmless defects, and advancing understanding of the effect of pores on mechanical properties (du Plessis et al., 2020). XCT has been instrumental in developing an understanding of the role of pore defects in the mechanical properties of metals, including AM metals in the last 15 years including but not limited to: Steuwer et al. (2006), Steuwer and Daniels (2011), Maire et al. (2007), Landron et al. (2011), Weck et al. (2008), Limodin et al. (2010), Toda et al. (2011), Lecarme et al. (2014), Nguyen et al. (2016), Krakhmalev et al. (2016), Patterson et al. (2018), Samei et al. (2020) and Hastie et al. (2021).

Although Hosseini et al. propose several mechanisms for varying properties between orientations and builds (including pores and grain boundary density), no direct evidence was provided (Hosseini and Popovich, 2019). To further explore the proposed mechanisms, we specifically studied pores undergoing uniaxial tension and ductile deformation to understand if, and how, pore defects impact deformation behavior of DED IN718. Broadly, pore deformation can be an important aspect of deformation, including the development of damage and failure. Our work develops a deeper understanding of how deformation progression alters pore shape and size (both individually and in aggregate) through direct observation and statistical image analysis during pre-failure deformation. Moreover, the *in-situ* deformation measurements presented here can be effectively used for image-based model verification, enhancing our confidence in the accuracy and precision of models that attempt to capture pore deformation during plastic deformation. This is particularly helpful for models, especially multiscale models, that directly represent microscale features, such as measured pores or simulated grain structures (Kafka et al., 2021; Yu et al., 2019; Herroitt et al., 2019; Li et al., 2019; Yan et al., 2018).

The manuscript is arranged into five main sections: Section 2 describes the materials and manufacturing methods used; Section 3 describes in detail the *in-situ* testing and imaging protocols; Section 4 provides results and discussion; Section 5 uses crystal plasticity modeling to determine the local grain orientation surrounding a pore, with a comparison of pore shapes between the numerical model and 3D imaging results. This section emphasizes the utility of direct, *in-situ* observation of pore deformation in relationship to micromechanical modeling. Finally, Section 6 provides concluding remarks, including thoughts on future studies.

2. Materials and methods

In this study, we focused on DED IN718, which was argon gas atomized to a particle size of 50 μm to 150 μm with a Gaussian distribution, before being used for the builds. All three builds studied here used the same batch of powder.

2.1. AM build details

Three single-track, "thin wall", builds using a DMG MORI LaserTec 65 3D Hybrid[1] were deposited on stainless steel grade 304 substrates. Thin walls are a simplified geometric case that minimize potential variables (such as removing the possibility of "lack of fusion" type defects) compared to a more complex build, while also enabling more direct observation of the build using side-on optics. The tool uses a direct diode laser, in this case operated at 1800 W, 1020 nm wavelength, and approximately 3 mm focal spot size. Each single-track build resulted in a wall nominally 120 mm long, 60 mm high, and about 3.5 mm thick. Argon shield and conveying gas at 7 L/min protected the melt pool while delivering powder coaxially to the laser. Three walls were built with different build patterns; each wall was built using a zig-zag scan strategy with a layer height of 0.5 mm and 1000 mm/min scan speed, but two walls shared a 18.0 g/min powder mass flow rate (PMFR) while the third had about a 27.0 g/min PMFR. Using the basic definition of Global Energy Density (GED) $GED = \frac{power}{(scanSpeed)(laserRadius)}$ (Kruth et al., 2005), the nominal GED of all three builds was 0.01 J/mm^2; however, because this is a thin wall build (and lacks hatch spacing), it may not be comparable to other GED measurements. Of the two walls with the same PMFR, one had no dwell time between layers and one had a 60 s dwell between layers. Differences in microstructure for similar thin wall structures with differences in dwell time have recently been reported (likely due to different cooling rate and residual heat), indicating that differences in mechanical performance may be expected (Guévenoux et al., 2020). Real-time thermal monitoring for these walls has in part been reported in Bennett et al. (2018). For these builds, the scan direction was taken to be along the length of the wall, the "hatch" or thickness direction is the thickness (although there is no hatching in the thin walls), and the build direction is the height away from the base plate, as indicated in Fig. 2.

After building, a 1 h at 1065 °C stress-relieving heat treatment followed by air cooling to room temperature was conducted, per AMS standard 5664F. It is important to note that this is a solutionizing heat treatment; a precipitation heat treatment was not conducted, although in practice is often used. The goal of the heat treatment was to reduce residual stress and enable removal of the build from the substrate without warping. This heat treatment likely solutionized precipitate phases from the build itself (predominately γ'' and Laves), but was unlikely to cause significant recrystallization (Sui et al., 2019). The specimens were eventually tested in the solutionized and air cooled state.

[1] Certain commercial equipment, software and/or materials are identified in this paper in order to adequately specify the experimental procedure. In no case does such identification imply recommendation or endorsement by the National Institute of Standards and Technology, nor does it imply that the equipment and/or materials used are necessarily the best available for the purpose.

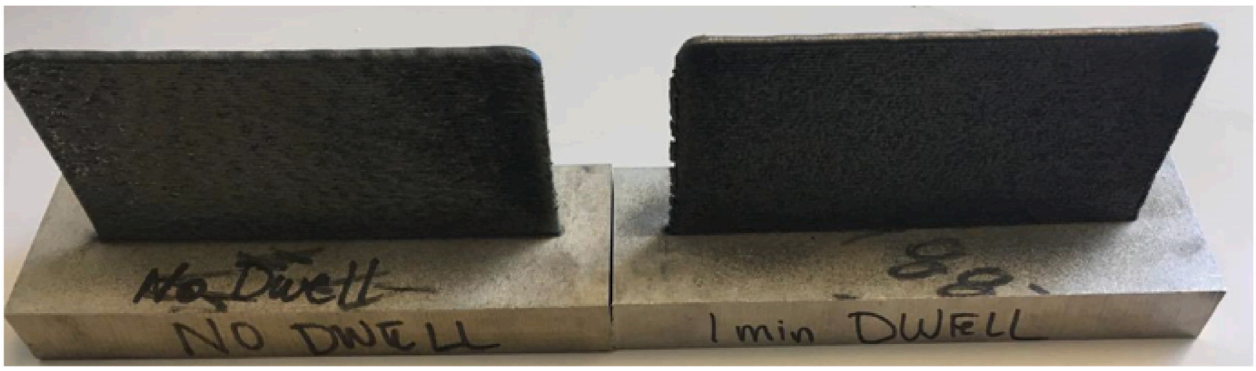

Fig. 1. A photography of two of the thin walls (Wall 3 (left) and Wall 2 (right)) that were then cut up to make miniature tensile coupons. Note there are noticeable geometry inaccuracies, even from this perspective.

A photograph of two of the thin walls prior to stress relief in Fig. 1 shows their as-built shape, including inexact geometric features such as slightly warped top and side surfaces and rounded corners that result from the process. This meant that any absolute real-space position measurements with respect to the programmed geometry had some unavoidable inaccuracy.

2.2. Specimen selection and preparation

Miniaturized ASTM E8 pin-loaded tensile coupons with nominal gauge section 2.5 mm long, 1.2 mm wide, and 0.8 mm thick (see Fig. 4) were designed for these tests. The geometry proved successful, in that most failures occurred in the gauge region, minimal strain was observed in the grip regions, and surface DIC indicated generally uniaxial strain states. Specifically, shear strains in the elastic region in the specimens were observed to be small (generally <5%) compared to the axial strains as measured by 2D-DIC, indicating relatively high uniaxiality. Specimens were exhumed from each wall using wire electric discharge machining (wire-EMD) to minimize disturbance of the material prior to testing. Wire-EDM can, however, leave a porous re-cast material layer, e.g. Markopoulos et al. (2020), which was observed in XCT to contain relatively higher porosity than the undisturbed material. The small size makes these specimens similar in concept to recent work in miniaturized testing of AM materials such as that of Benzing et al. (2020), and builds a case for the utility of sub-scale mechanical testing for AM materials. The smaller geometry might inherently result in different measurements than full size coupons, although in some cases miniaturized specimens may provide similar results (Anderson et al., 2017). In any case, for this study using small specimens was necessary in order to understand the possible distribution of properties within each wall. With little *a priori* knowledge of the distribution of properties within the walls, a Sobol sequence was used to define the points at which the specimens were collected from the walls. The Sobol sequence maximized the information gathered on the underlying spatial distribution of properties measured within the walls (Burhenne et al., 2011), which reduces testing requirements when compared to, e.g., random sampling. To test for anisotropy, half the coupons were exhumed with the gauge section parallel to the build direction and half perpendicular to the build direction. To maximize the similarity, in terms of processing history, between the horizontal and vertical specimens and eliminate possible differentiating variables, the roughly 3 mm thick wall was sectioned longitudinally to produce two 0.8 mm to 1 mm thick sheets (changes in thickness resulted from unavoidable warping during removal from the build substrate). Horizontal and vertical specimens were then cut from the same coordinates of each sheet, such that the distance between gauge sections in the precursor material was minimized. Due to the symmetric nature of the single-track thin wall, through-thickness variability was minimal and the specimens are generally similar between sides as confirmed by grain,

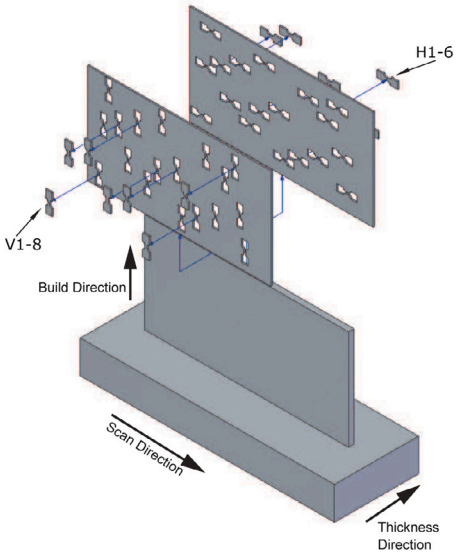

Fig. 2. Coupon locations in each thin wall (single laser track) build, with two labeled examples.

pore, and mechanical properties comparisons. This specimen extraction and overlap-gauge-section concept is shown schematically in Figs. 2 and 3. A local specimen coordinate system with x aligned along the tensile axis, y parallel to the front/back plane of the specimen, and z into the thickness direction was used to simplify analysis. Thus, for the horizontal specimens local x strain implies strain in the scan direction, whereas for the vertical specimens, x strain implies strain in the build direction relative to the build coordinate system.

2.3. Surface preparation

To remove possible effects of the wire-EDM specimen cutting procedure, the specimens were chemically processed after machining. All specimens were immersed for approximately 90 min in Kalling's Etchant (a proportionate mix of 5 g $CuCl_2$ + 100 cc HCl + 100 cc Ethyl alcohol Small et al., 2017), which removed about 50 µm (0.05 mm) of surface material from all faces. Prior to immersion, both pin-connector ends of each specimen were coated in etch-resist, which was subsequently removed. This procedure proved insufficient to completely eliminate the re-cast wire-EDM layer, and some amount of surface porosity likely due to the wire-EDM process was still observed in the XCT results.

After this, caliper measurements of all specimens were taken, with three repeat measurements at three locations along the gauge section in

Table 1
Summary of specimen labeling scheme.

Position in label	Possible entries	Description
First	H/V	Horizontal or vertical
Second	1/2/3	Wall number: 1 = 27 g/min PMFR, no dwell; 2 = 18 g/min PMFR, 60 s dwell; 3 = 18 g/min PMFR, no dwell
Third	1–11, 20, 30, 40, 50, 60	Specimen number within wall, sorted by Sobol order

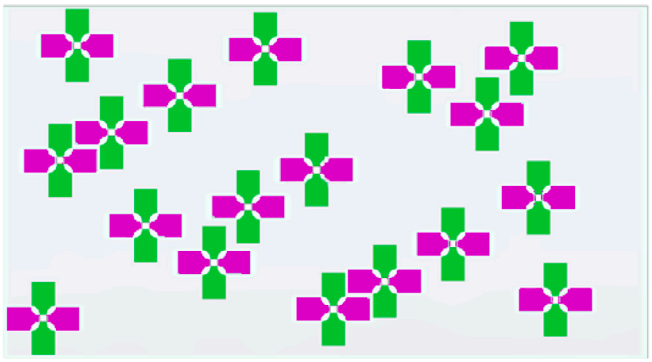

Fig. 3. Relative locations and orientations of tensile specimens. Green are vertical (long axis aligned with the build direction, which is vertical in this schematic), and purple are horizontal (long axis along the scan direction).

each dimension (width measured with calipers, thickness with micrometers). These were used to compute cross-sectional area for engineering stress calculations prior to conducting XCT measurements. Dimensional uncertainty associated with caliper and micrometer fidelity, and its impact on stress uncertainty, was propagated from these measurements to the stress–strain curves. An image of the specimens prior to testing is shown in Fig. 5, where each specimen is uniquely labeled using a letter/number convention that will be referenced in later sections. The first character, H or V, refers to the orientation (horizontal or vertical) with respect to the build direction. The second character refers to the wall: 1 = 27 g/min (0.45 g/s) PMFR, no dwell; 2 = 18 g/min PMFR (0.3 g/s), 60 s dwell; 3 = 18 g/min (0.3 g/s) PMFR, no dwell. Finally, within each wall slice the specimens are numbered in accordance with the Sobol sequence, thus higher numbers provide decreasing returns in terms of information regarding the spatial distribution. The numbers that end in a 0 were manually added after the sequencing to probe the extremes of the build, either at the top or edges of the build, where we suspected different properties might exist. The numbering scheme is summarized in Table 1.

The final stage of specimen surface preparation was to apply a speckle pattern to the gauge sections, to enable full-field digital image correlation measurements of the deformation. A black background with white speckles was generated using a solution of 6 μm alumina powder in ethanol applied to a still-tacky layer of matte black spray paint. Some amount of unavoidably clumping meant that the observed particles tended somewhat larger than the powder itself. Our preliminary testing showed that the resulting pattern had an ideal minimum subset size of about 60 μm when using the optical setup deployed during mechanical testing.

3. Mechanical testing

Specimens were tested *in-situ* in ambient air at Argonne National Laboratory's Advanced Photon Source Beamline 2-BM. A custom-built, remotely controllable, single-sided, miniature screw-actuated load frame (Wejdemann et al., 2010; Efstathiou et al., 2010) was used to conduct tensile loading within the hutch, as shown in Fig. 6. Quasi-static testing was conducted under displacement control, such that a nominal initial strain rate 5×10^{-4} s^{-1} was achieved based on initial specimen length and a continuous crosshead displacement rate. This was obtained with a crosshead displacement rate of 1.25 μm/s, kept constant during all subsequent deformation steps for both the continuous and interrupted loading cases described below. At these strain rates, this material is relatively rate-insensitive, so the steadily decreasing strain rate caused by using a fixed displacement rate was assumed to have a minimal influence. Displacement was applied only one side of the specimen, while the other side was held fixed, resulting in the gradual motion of the specimen through the frame of view of the DIC camera as well as motion of the volume inspected by XCT. Some motion mitigation for XCT viewing was attempted, although with this hardware configuration it was ad-hoc and no assurance can be made that the field of view does not change during the large deformations that the specimen undergoes.

3.1. Continuous and interrupted loading

Two different displacement-controlled testing protocols were used. An interrupted *in-situ* modality was employed to enable XCT imaging at pre-defined points during deformation (similar to, e.g., Maire et al. (2007), Carlton et al. (2016), and Kim et al. (2020), although specifically designed for our specimens), and a continuous loading through failure was used to enable more direct comparison to standard E8 tests of IN718. The concept of incremental and continuous *in-situ* testing is not new, see for example (Maire et al., 2007) for an example with a specialized aluminum metal matrix composite, but still deserves thorough description. In the former, displacement was applied at a constant rate to the specimen until an engineering stress of 575 MPa was reached. This was usually quite close to the yield stress. At this point, deformation was stopped for approximately 8 min (about 480 s). This allows about four to five minutes of creep, during which time settings, file paths, etc. are manipulated as required. At this point, the creep rate is low enough to conduct a 3.5 min scan without specimen motion causing artifacts (i.e., we computed that on average a pore would move less than 0.65 μm, one voxel, during the scan). After the scan, displacement was increased again until stress had increased by 75 MPa, at which point another pause followed by another scan was conducted. This procedure of load–wait–scan was repeated until the ultimate tensile strength was reached. At this point, due to the more rapid change in behavior during the softening regime, scans were taken after every 15 MPa of load drop. The displacement versus time graph is shown in Fig. 7 is an example to illustrate the displacement history common for "start–stop" specimens. Although the details of the test protocol were designed specifically for our test conditions, a similar strategy was used by Yvell et al. (2018) which showed little difference for nickel-rich steel between stop–start testing and continuous testing in terms of overall response. In two cases, rupture occurred during either the primary creep hold time or during scanning. The continuous loading case was simply a standard tensile test to failure, with XCT data collected before the test started and after failure. Although prior literature is understandably scare on the impact of interrupted *in-situ* testing on general deformation behavior and material performance of DED IN718 specifically, our results below seem to indicate limited difference for IN718 between interrupt and continuous testing, although we were unable to confidently isolate this as a variable due to the heterogeneous nature of the AM material in this study. In this case, we must be somewhat careful to avoid excessive comparison between specimens tested with interrupted versus continuous loading.

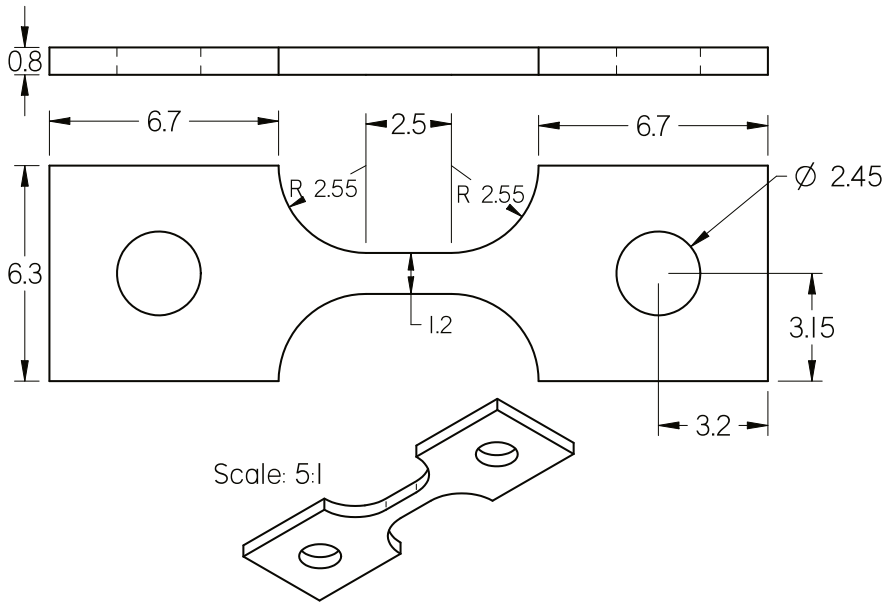

Fig. 4. Details of nominal miniature specimen geometry, dimensions in mm.

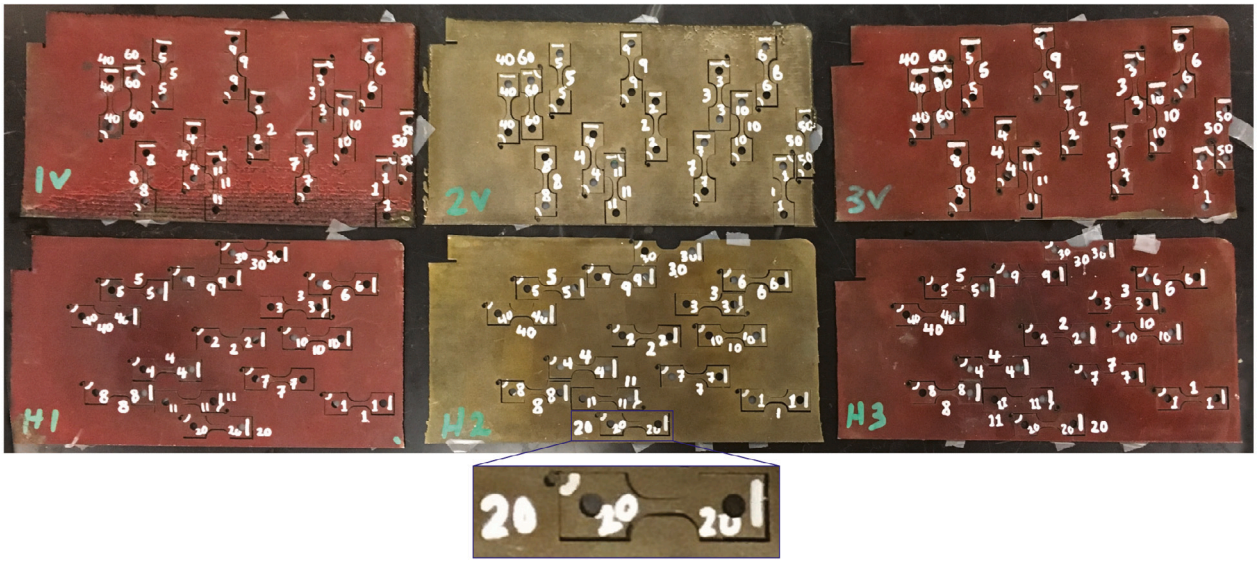

Fig. 5. Labeled specimens in their respective thin wall slices prior to testing, and a more detailed view of one particular specimen showing real geometry in the build plate after wire-EDM machining.

3.2. Surface strain measurement with digital image correlation

During deformation and at all times other than during an XCT scan (when the specimen was rotated and thus not observed by the camera), speckle pattern images of the specimen surface were collected with a Point Gray Research Grasshopper3 camera, sensor size 3376 × 2704 pixels, at 1 frame/s and with exposure time 0.5 s. An Infinity K2/DistaMax long distance microscope with K2 Close-Focus Objective and CF-2 optic was used to provide detailed images of the gauge section of the miniature test specimens. A LED light panel with custom light directing hood was used to avoid influencing the x-ray detector. LED lighting does not significantly heat the specimens or surrounding air. Specular reflections were mitigated with cross-polarization, as suggested by LePage et al. (2016). The use of this rather bulky collection of DIC equipment was made possible by the space available in the synchrotron hutch, which is generally much larger than in lab-scale XCT systems. Two-dimensional digital image correlation with the VIC 2D software package (Solutions, 2018) was used to compute surface displacement after testing. Details of the DIC settings that generally provided good quality correlations for these images are provided in Table 2. Of note, the tele-microscope lens does not have fixed f-stops and instead uses an adjustable field iris. We adjusted it to achieve satisfactory image quality, lighting, and depth of field for our speckle pattern and illumination. Also note that, the confidence intervals on zero-displacement images will be somewhat smaller than for images taken during deformation (as an approximation, the highest observed strain rate would result in about a half-pixel of motion while the shutter is open). Out of plane motion was minimal, even during necking the maximum possible spurious biaxial strain due to Poisson effect is approximately 1.5×10^{-3}, which is much less than the overall strains at the point of maximum out of plane motion. In practice, this maximum is far from what is observed, as width reduction is on the order of 50%. From the displacement, total strain was computed using both a local and a global approximation from the measured

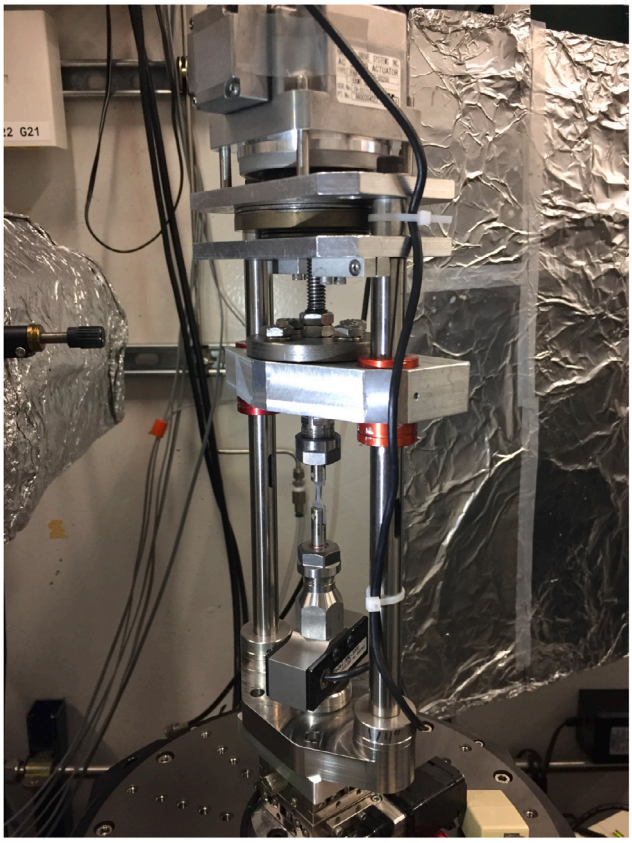

Fig. 6. The miniature screw-actuated load frame used for mechanical testing, as installed on the rotary stage of Beamline 2BM-B. A specimen can be seen mounted in the pin-style clevises, themselves held with collets, which are attached on the bottom to the load cell and on the top to the movable crosshead.

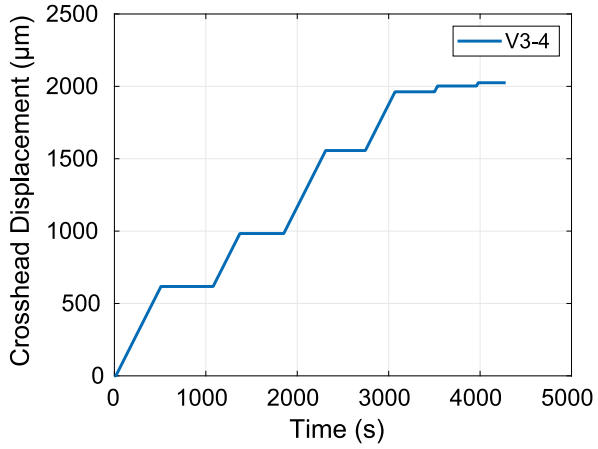

Fig. 7. Crosshead displacement versus time for specimen V3-4, as an example of the "start–stop" or interrupted *in-situ* loading pattern. Constant displacement rate during crosshead motion is also demonstrated.

displacements (both were used and compared both in VIC2D and in a custom MATLAB script to help ensure accuracy). For some specimens, load frame displacement was tracked and used to cross-verify the DIC results, although in all cases DIC strain measurements are reported. These DIC displacements/strains were registered against load cell readings by minimizing the difference in time stamp to produce load vs. displacement as well as engineering stress versus engineering strain.

Table 2
Optical and VIC2D DIC settings used to compute surface displacements, reported as suggested by Bigger et al. (2018). The 95% confidence intervals are the mean value for a representative zero displacement image pair (from V2-3) assuming normally distributed error.

Optical parameter	Value
Camera body	Point Gray Research Grasshopper3
Sensor size, px	3376 × 2704
Lens	Infinity K2/DistaMax
Objective	K2 Close-Focus with CF-2
Working distance, mm	approx. 300
Image scale, pixels/mm	approx. 518
DIC parameter	**Value**
Software	VIC-2D Version 6.06, build 665
Subset size	35
Step size	7
Subset weights	Gaussian
Interpolation	Optimized 6-tap
Criterion	Normalized squared differences
Mode	Incremental
Consistency margin, maximum margin, px	0.02
Confidence margin, maximum margin, px	0.05
95% CI for displacement, px	[0.012, 0.081]
Matchability threshold, maximum margin	0.1
Strain computation filter size, px	15
Strain measure	Lagrange
95% CI for strain	[−8.05e−05, 6.57e−04]

3.3. XCT observation of porosity

Tomographic measurements of the specimens were conducted at the 2-BM beamline of APS at ANL. The load frame noted above was mounted on the top of a rotary stage. In a tomography scan, the load frame and specimen held within it were rotated through 180-degrees while an X-ray detector behind the specimen acquired 1501 projection images of the specimen. The X-ray detector was composed of a 20 μm thick LuAG:Ce X-ray scintillator, a 10× Mitutoyo long-working distance optical objective lens, and a PCO Edge5.5 sCMOS camera, which gave an effective 0.65 μm pixel size. The broadband, white-light X-ray from the source was filtered to provide an illumination beam with peak energy about 60 keV. In the scans, the two supporting arms of the load frame blocked about 20 degrees in the total 180-degree angle range. The images taken in this black-out angle range were discarded in the tomographic reconstructions, meaning that only 160 degrees of data were used for reconstruction. A custom reconstruction technique was used to mitigate the impact of these dropped frames, the details of which can be found in the related code and data publication [dataset] (Kafka et al., 2022). The exposure time of projection images was 100 ms (0.1 s), and each tomographic scan took 3 min scan time and 0.5 min scan preparation overhead time. This system is shown schematically in Fig. 9. For all specimens, a field of view was selected that started about 0.150 mm below the upper fillet and extended 1.3975 mm toward the lower fillet, capturing the upper two-thirds of the gauge section, at least before deformation began. Because the load frame applies single-sided displacement, the field of view was translated half the total crosshead displacement at each step to roughly maintain the field of view. Specimens tested using the continuous loading protocol were scanned before testing and the two sides of each broken specimen were scanned after failure using all the same settings.

Tomographic reconstruction was conducted using a customized version of Tomopy 1.0.1 (Gürsoy et al., 2014). The modifications were a correction of a coding error that results in the program hanging during multi-processor operation and an added output to directly make an 8-bit tiff image rather than the standard 16-bit output (to save disk space, as there was no noticeable difference in final 3D image quality for these specimens). An example initial projection image is shown in Fig. 8(a). Projection images were processed in a high-throughput, parallel environment based on a combination of BASH and Python

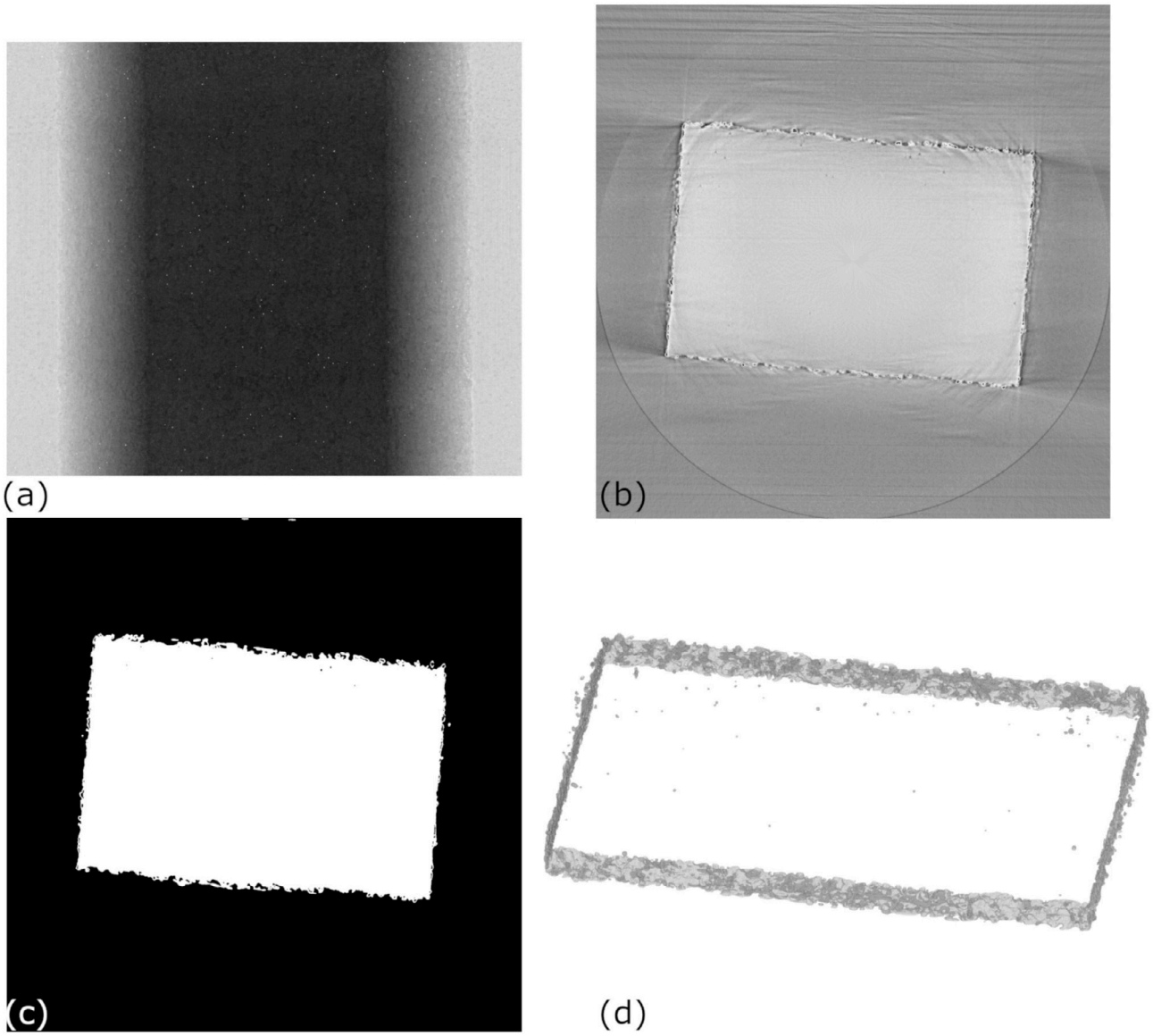

Fig. 8. (a) example projection image (reproduced here with an "equalized" histogram to enhance visibility, and without bright and dark field corrections), (b) gray-scale reconstruction slice, (c) filtered and thresholded slice, (d) filtered and thresholded 100 slices around the slice shown in part (c).

scripts. In Tomopy, the projection images were normalized, followed by phase retrieval, stripe removal, and a final renormalization. After reconstruction using the gridrec algorithm, range adjustment, outlier removal and ring removal were conducted before saving the tiff image stack (Fig. 8b). Next, a series of edge-preserving, smoothing filters to reduce noise and enhance contrast between the material and pore phases were applied using the MATLAB Image Processing Toolbox (version 2018b) with a series of *localcontrast*, Wiener, and median filters. Both 2D and 3D versions of the filters were tested, and largely similar final 3D results achieved with both. So the faster 2D filters were chosen and all reported images use the same set of 2D filters. After filtering, the *graythresh* and *imbinarize* functions were used to binarize the images, differentiating the volume into two phases: surrounding air/pores and metal (Fig. 8(c) and (d)). Data from intermediate processing steps can be reproduced using the associated dataset [dataset] (Kafka et al., 2022). The voxel edge length was 0.65 μm, giving a minimum detectable pore size, if we assume that two darker voxels in each direction would be detectable, of about 2.197 μm^3.

Overall descriptive parameters were extracted from the binary images of the material using the techniques developed in Garboczi and Hrabe (2020a,b) and Bain et al. (2019). In order to focus upon the primary features of interest, DED-derived pores, several more processing steps were required for these images. The images were first cropped and the exterior air spaced turned gray. Surface pores produced by the wire-EDM process were removed by conducting 30–50 dilation steps of this gray region. The gray region was turned black, leaving only the internal pores. Some of these pores are likely reconstruction "ring" artifacts, caused by the slightly reduced contrast in the *in-situ* XCT images due to interference from the load frame. To ensure these were not included in pore evolution statistics, each pore was evaluated as to whether or not its 3D shape could be expanded in spherical harmonic functions. Those that could not be so expanded were removed from the analysis as probable artifacts, because real pore are generally roughly spherical (recall there are no lack-of-fusion defects). Spot checking with 3D images of these pores confirmed this hypothesis. The parameters L, W, and T were computed for each pore analyzed, where L is the longest distance across a pore, W is the longest

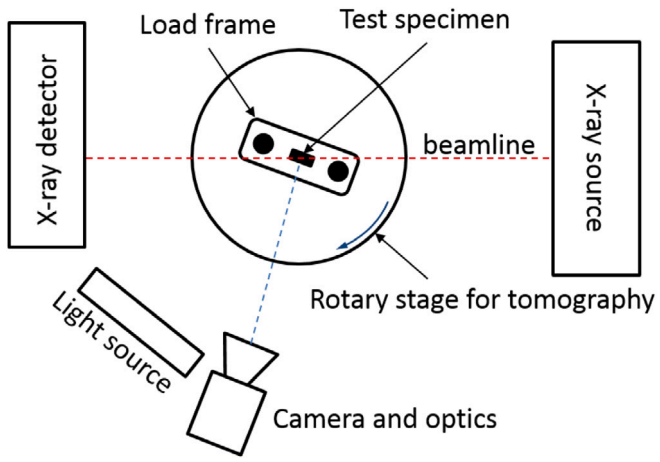

Fig. 9. Schematic diagram (not to scale, top down view), of the specimen location with respect to the DIC camera and x-ray beam.

distance that is also perpendicular to L, and T is the longest distance that is also perpendicular to both L and W. The bounding box extents in image coordinates were computed and denoted x, y, and z, where z is the loading direction.

4. Experimental results

4.1. Stress–strain curves

For each thin wall, at each point in strain the stress values of all the H or V specimens were averaged together. The "average" engineering stress–strain curves with shadowed regions representing ±1 standard deviation (SD) are shown in Fig. 10; (a) wall 1 (27 g/min PMFR, no dwell, continuous testing), $N_V = N_H = 10$, (b) wall 2 (18 g/min PMFR, 60 s dwell, stop–start testing), $N_V = 4$, $N_H = 3$, and (c) wall 3 (18 g/min PMFR, no dwell, stop–start testing), $N_V = N_H = 4$. Because stress depends on cross-sectional area, and our area measurement introduced uncertainty, we have also plotted the mean of the extents of area-measurement-based uncertainty, propagated from caliper and micrometer uncertainty, in Fig. 10 (computed similarly to how the "average" stress–strain curves themselves were computed). Data for some specimens were deemed to be unreliable (e.g. poor or failed DIC correlation, usually due to speckle pattern debonding) or simply missing due to operational challenges, and those specimens are excluded from the analysis. Recall that a stress-based criterion was used to determine when to scan. This means that there is some spread in the strain values at which scans are taken. Thus, for wall 2 and wall 3, there are some points where the stress measured during loading and stress measured during hold periods are sometimes averaged together. This results in the increased variability and decreased smoothness of the averaged stress–strain response of walls 2 and 3 compared to wall 1. The curves in Fig. 10 show that in general there are noticeable differences between orientations and between processing conditions. In wall 1, these differences are statistically significant throughout most of the stress–strain curve; walls 2 and 3 have somewhat artificially increased SDs, so are not statistically significant but this might be because of the added variability from averaging over the hold and non-hold periods as explained above. Also note that while a mean line is provided, this does not represent any particular specimen and is included to give a sense of the overall material performance and variability. Specific examples are given in 12. The full stress, strain, displacement, force and more is provided in the associated data publication, along with the techniques used to create these "average" representations [dataset] (Kafka et al., 2022).

4.2. Horizontal versus vertical stress–strain response

To quantify the differences noted between H and V in the stress–strain curves above, common parameters have been extracted from each. The commonly used single-point descriptors of the stress–strain response elastic (Young's) modulus, 0.2% offset yield stress (σ_y), ultimate tensile stress (UTS), and maximum measured elongation are used to make these comparisons. Most mean values are within one standard deviation of the others, but some trends seems to appear that may be of practical interest if not statistical significance. For instance, in processing condition 1, horizontal specimens tend to have suppressed yield stress and ultimate stress, but higher elastic moduli than their vertical counterparts. This does not appear to be the case for the other processing conditions, but a more limited sample size confounds the analysis somewhat; modulus is higher for horizontal specimens in processing condition 3 compared to vertical specimens, but marginally lower in processing condition 2. Yield and ultimate stress appear broadly similar for horizontal and vertical specimens in processing conditions 2 and 3, although horizontal is somewhat higher on average. Maximum elongation appears to be lower for the horizontal configuration across all processing conditions, in keeping with the common trend that higher yield and ultimate stress often correlate with lower elongation and toughness. Similar trends as observed here are noted in the review of Hosseini and Popovich (2019), in particular higher elastic modulus for horizontally oriented specimens compared to the vertical specimens. Further details including box-and-whisker plots are given in Appendix B.

The spread of results and relationship with location may be indicative of the impacts of both microstructure and defects such as pores. However, fully developed necking occurs and ductile response of the material appear to be relatively un-impacted by pores at the low overall volume fraction observed in these samples, so this is unlikely to be a strong factor. As an example, the distribution of pores and porosity for H3-4 and V3-4 are shown in Fig. 11. More recent work has also indicated that microstructure, rather than pores, is likely dominant over pores for porosity levels as low as is observed here, cf. our results to those in Watring et al. (2022), as an example of the scale of porosity required to govern response of AM IN718 (the comparison is imperfect, however, because Watring et al. (2022) used laser powder bed fusion material with much smaller grain size).

These mechanical test data provide the context with which the following pore deformations can be more readily understood. Further plots are provided in the Supplemental Materials, showing the average stress–strain behavior and location dependency (Supplemental Information 1 and Supplemental Information 2). The complete data are provided in the accompanying data publication [dataset] (Kafka et al., 2022) for all specimens tested. For a more thorough analysis of thin-wall mechanical properties variations in the vertical configuration and with different post-build heat treatments, similarly designed studies have been conducted and focus on relating thermal conditions to mechanical test results (Glerum et al., 2021; Bennett et al., 2021, 2018).

4.3. Deformation observations

Stress–strain curves tested with the interrupted protocol for position 4 in walls 2 and 3 are given in Fig. 12. For reference, a wrought IN718 test result for annealed material (982 °C anneal, followed by air cooling according to the material supplier) using the same specimen geometry and equipment is plotted as well. The heat treatments used for the wrought and AM material are similar, though not identical. The surface roughness of the wrought specimen was slightly higher, which may have driven earlier failure but is unlikely to have increased stiffness and yield strength as dramatically as shown in Fig. 12. In both cases, precipitation strengthening during heat treatment is unlikely to have occurred, although elemental segregation has been known to alter the heat treatment dynamics of AM materials (Lass et al., 2017). All the AM

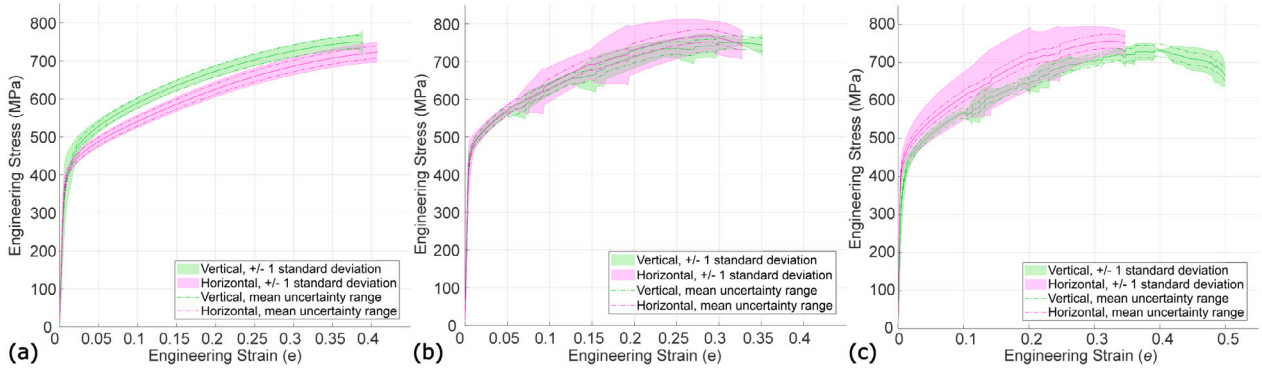

Fig. 10. Averaged engineering stress–strain results for (a) wall 1, continuous testing, (b) wall 2 (60 s dwell), stop–start testing, (c) wall 3 (no dwell), stop–start. The light background is one standard deviation spread on the data, and the dot–dashed lines represent uncertainty in stress due to uncertainty in cross-sectional area measurement. This uncertainty was computed for each specimen: the differences between specimens are small and the mean uncertainty is shown. This figure highlights the variability between specimens and differences between H and V. Note: due to the specimen-to-specimen variability, the mean line does not represent any one specimen, but rather the general behavior of the set tested.

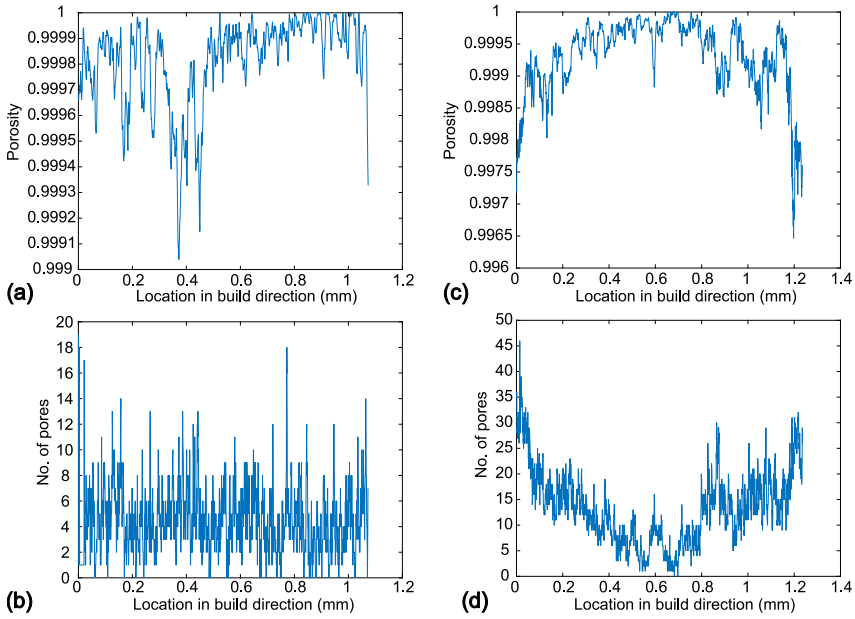

Fig. 11. Plots of porosity (i.e., ratio of material to voids, $0 \leq x \leq 1$) and pore count (with smallest detectable pore about $2.197\,\mu m^3$) versus height in the build direction computed on a slice-by-slice basis from the X-ray CT images. (a) H3-4 porosity, (b) H3-4 pore count, (c) V3-4 porosity, (d) V3-4 pore count. This indicates inhomogeneous distribution of porosity and pores throughout the build, although at relatively small amounts of both. Pore size analysis is shown later, in Section 4.4.2 and Appendix C.

coupons are tougher than the wrought material, with longer elongation but lower yield/ultimate stress and stiffness.

Two frames of deformation throughout the history of two specimens are given as an example of the data collected during *in-situ* monitoring. These pores change shape during the tension test, as shown in Fig. 13; here, pores at the onset of plasticity and near failure are shown, at the stress/strain points indicated by the corresponding number (1) through (4) in Fig. 12. Although comparing between surface and volumetric phenomena is imprecise in these experiments, the equivalent 2D DIC strain maps recorded just prior to starting the XCT scan for each of these four cases (H2-4 at 575 MPa and 700 MPa, and V3-4 at 575 MPa and 650 MPa) are provided in Fig. 14. Videos showing the deformation are provided in Supplemental 4, and the complete datasets are provided in the associated data publication [dataset] (Kafka et al., 2022). Precise registration between the XCT volume and the DIC data stream was not conducted. However, in general, the XCT images are slightly to viewer's right of center in the gauge region in both cases, and can be qualitatively compared to the DIC. From the DIC data, specimen V3-4 appears to undergo more uniform deformation, and once necking occurs has a larger necked region compared to specimen H2-4. Likewise, necking can be seen in the XCT images, although relating particular features is not possible. In images 2 and 4, localize deformation has caused non-uniform stresses, i.e., the development of stress triaxiality, within the necked region. Previous literature has studied this effect, as the effects of stress triaxiality are important to understand the detailed progression of damage, e.g., Weck et al. (2008), Landron et al. (2011) and Maire et al. (2008). Future work focused on post-necking damage rather than the general progression of deformation might use these data to more thoroughly study the impact of triaxiality in void-based damage mechanics in DED IN718.

4.4. Defect tracking: observations and measurements

The primary use of XCT in this study is to track and measure pores as the metal deforms. The information thus gathered can be used to better understand the deformation and failure mechanisms, and the roles that pores might have in these. Overall porosity was also computed from the XCT data and found to be less than 0.1%, and can be considered "fully dense" for AM materials.

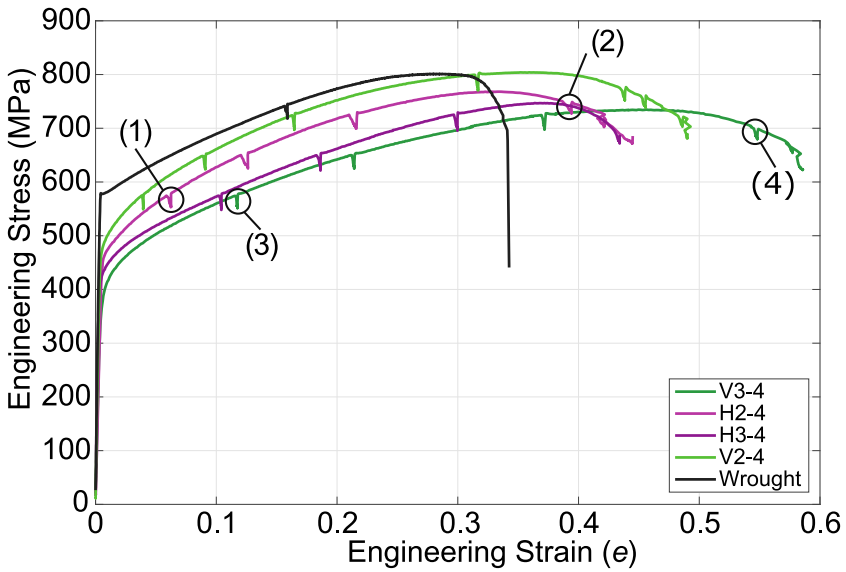

Fig. 12. Stress–strain plot of four *in-situ* test specimens at location 4 in both vertical and horizontal configurations (V vs H) and walls 2 and 3. For reference they are compared to the behavior of a wrought, annealed IN718 specimen tested on the same equipment with the same specimen geometry (black line). Points called out on these curves correspond to the XCT scans shown in Fig. 13.

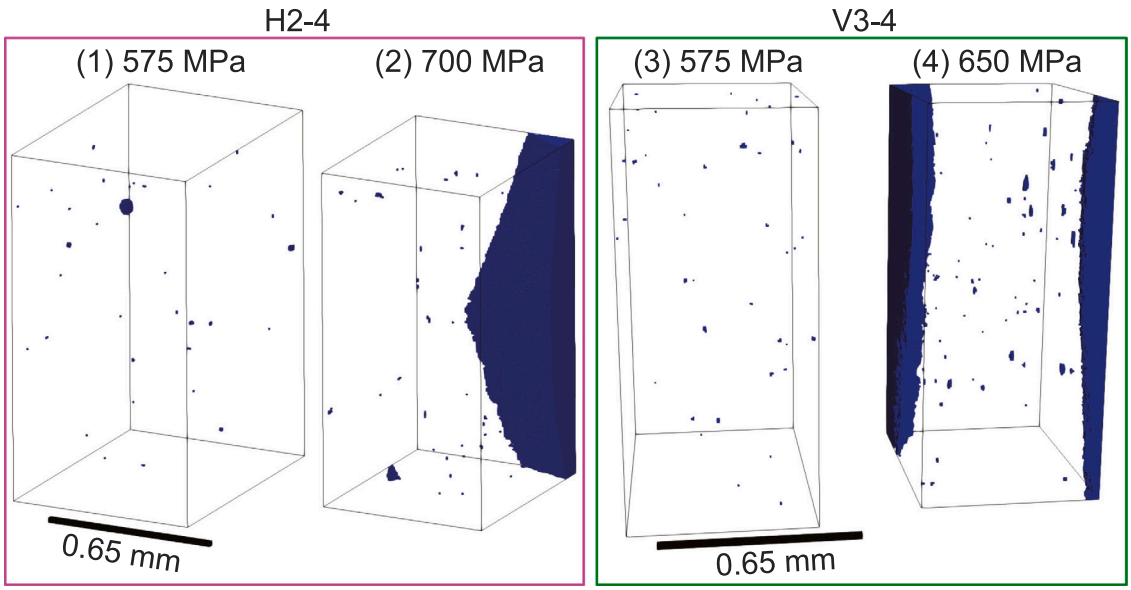

Fig. 13. Two deformed configurations for specimens H2-4 and V3-4 (at the same relative position in each build), one at the onset of plasticity (left side) and the other at the final scan before failure (as indicated on the stress–strain curve in Fig. 12 by the last drop in stress before failure). The large blue bands are the encroaching edges of the specimen as it thins during deformation. Notice that in the vertical configuration, where more elongation occurs, the pores have deformed substantially before failure but in the horizontal case similar pore evolution has not occurred, at least by visual inspection for this case.

4.4.1. Single pore deformation

The deformation progress of single pores throughout the strain-history can be tracked in the XCT data, for example as shown in Fig. 17, which demonstrates a series of four subsequent pore states for a particularly large pore in specimen H1-8. XCT data was not registered between data steps, and the field of view changed as the material deformed. However, in the case, the pore stayed within the field of view throughout these four frames. The stress-time points at which these snapshots were taken are circled in the stress-time curve shown in Fig. 16; the subset image shows the relative location of this pore of interest within a sub-volume of the gauge region. Plotting stress versus time in Fig. 16 emphasizes the creep region during the XCT scan. The stress trace also increases rapidly from the post-creep value to the pre-stop value (within a couple of MPa generally) indicating stress recovery upon continued displacement. This recovery can also be seen in the stress–strain plot, e.g. Fig. 12. Another, similar set of four snapshots during deformation is provided in Fig. 15, which shows a pore in specimen H2-4 undergoing a similar process. These image for Fig. 15 are rendered from spherical harmonic series expansion of the XCT voxels providing a somewhat smoothed appearance. We propose that the plastic flow in a single crystal results in the observed deformation in these cases. For large pores that are easily isolated and tracked between scans, we observe that deformation causes the pore to elongate in the direction of load, while narrowing in the other two orthogonal directions (see Figs. 15 and 17). This effect is quantified in Table 3, which confirms the observation, and shows that length in the load direction (z-extent, as measured by an external bounding box aligned along the image coordinates) increases while y-extent and x-extent

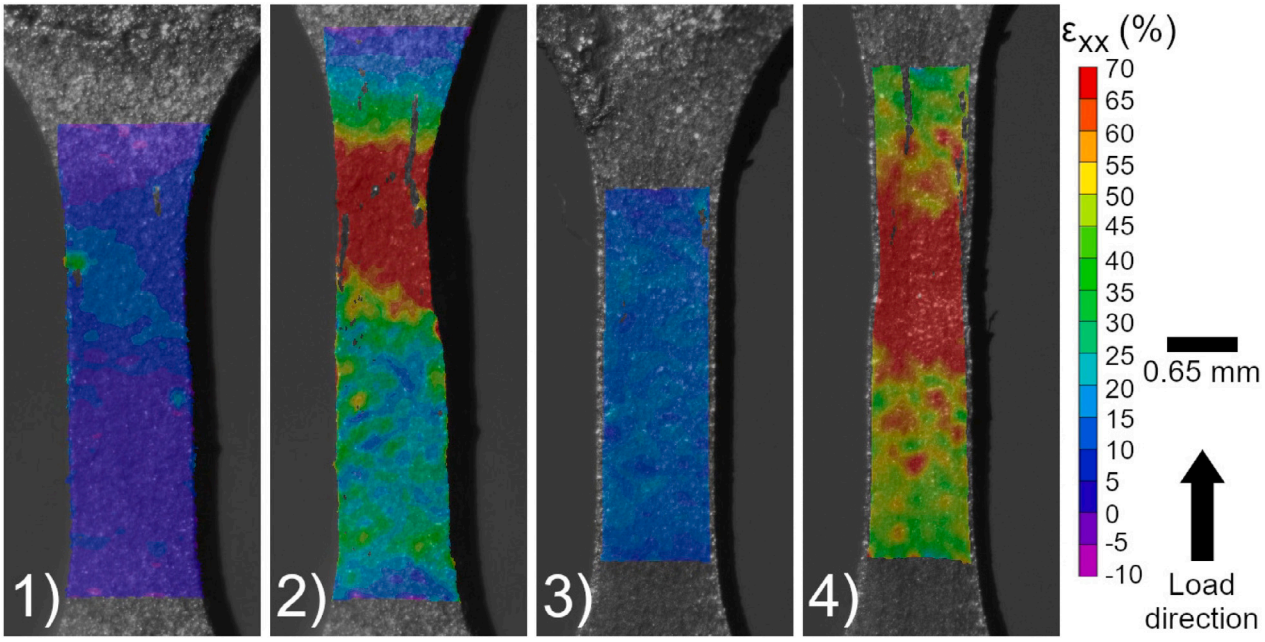

Fig. 14. DIC surface strain maps showing deformation at two different load steps for two specimens (see also Supplemental 4); although individual strain concentrators are not possible to see, the same overall trend of uniform elongation followed by localization as expected and seen in the XCT images is observed. (1) H2-4 at 575 MPa applied engineering stress, (2) H2-4 at 700 MPa, (3) V3-4 at 575 MPa, and (4) V3-4 at 650 MPa. (1) through (4) correspond with the XCT images labeled (1) to (4) in Fig. 13; XCT volumes are roughly 1.2 mm in height, located 0.15 mm below the end of the upper fillet.

Table 3
H2-4 single pore geometry evolution. The pore in question can be seen in Fig. 15, as well as in the upper-middle of Fig. 13H2-4(1), however subsequent loading after 725 MPa moved this pore outside the field of view, as can be seen in Fig. 13H2-4(2) taken after UTS (hence stress lower than 725 MPa). All lengths are in μm.

	0 MPa	575 MPa	650 MPa	725 MPa
x-extent	47	46	43	42
y-extent	49	50	45	44
z-extent	50	56	62	70
L/T	1.09	1.22	1.46	1.71
Volume (μm^3)	58 312	60 088	60 243	61 592

decrease, causing the pore to become more oblong as described by the L/T ratio increasing (where L is the longest line that can be drawn through the pore and T is the shortest line orthogonal to that). Overall, however, the pore tends to slightly increase in volume. In both cases, narrowing is not necessarily consistent throughout the circumference, which is indicative of the anisotropic nature of a single crystal in which the pore is likely embedded.

In general, this pore deformation is consistent with previous literature. For instance, Weck et al. (2008), found similar pore elongation for similar sized pores during deformation of pure copper and a copper–aluminum alloy. The density of pores in their work was specifically designed and observed to result in pore coalescence at higher levels of deformation, which was not observed at the porosity and pore spacing in the DED IN718 tested here. However, the current work focuses more on overall deformation behavior than specifically on damage and failure and more detailed study may potentially make further progress in the damage of these materials.

4.4.2. Quantitative measurements of pore deformation

Observing a single pore deforming provides an indication of the general tendency of pores to elongate, but to generalize and compare between specimens we also analyzed the overall behavior of all detectable pores. Overall shape evolution statistics are given for four example specimens; the shape change in terms of the average lengths in x, y, and z are given in Fig. 18. This figure shows that the average pore behaves similarly to the individual large pores shown above. Pores on average tend to elongate in the direction of uniaxial loading (z), while contracting to a greater or lesser extent in the two orthogonal directions (x and y). The data in each graph in Fig. 18 is an average over a minimum of 80 and a maximum of 390 pores. This is large enough of a data set to meaningfully construct averages, but also small enough that results may vary simply as different pores enter, or more commonly leave, the field of view of the XCT image as the specimen stretches and field of view changes slightly. The change in number of pores as a function of load level, shown in the tables in Appendix C, represents this finite field of view effect. Hence some stress-level-to-stress-level variability within each specimen is expected.

One trend seems to be that the vertical specimens tend to undergo greater pore elongation, and experience an especially pronounced increase in elongation in the post-UTS (localization) region. Vertical specimens tend also toward greater elongation-to-failure, as noted in Section 4.2. This correlation may suggest that ductile mechanisms of deformation perhaps less closely spaced grain boundaries allowing for more free dislocation movement may involve greater pore shape change in the vertical configuration. These factors may also be related to anisotropy in the mechanical response observed above. Pores in the 60 s dwell time wall (Wall 2) tend to undergo larger elongation as well, which may be related to differences in solidification cell structures that could develop differently because of different cooling rates and overall thermal conditions. In all cases, the volume of pores tend to increase with deformation, i.e. void growth, which is a commonly understood mechanism of ductile deformation.

The large pore shown in Fig. 15 was approximately 10 times the volume of next biggest pore. This pore was not found in the other loading steps (i.e. it moved out of the field of view). The presence of this pore would skew the number-based averages of L, W, T, <x>, <y>, and <z>. The average data for graphed in Fig. 18 do not include this one big pore. Appendix C provides complete, detailed information regarding the average pore deformation in Tables C.5 (similarly, with the large pore removed for the first four entries), C.6, C.7, and C.8.

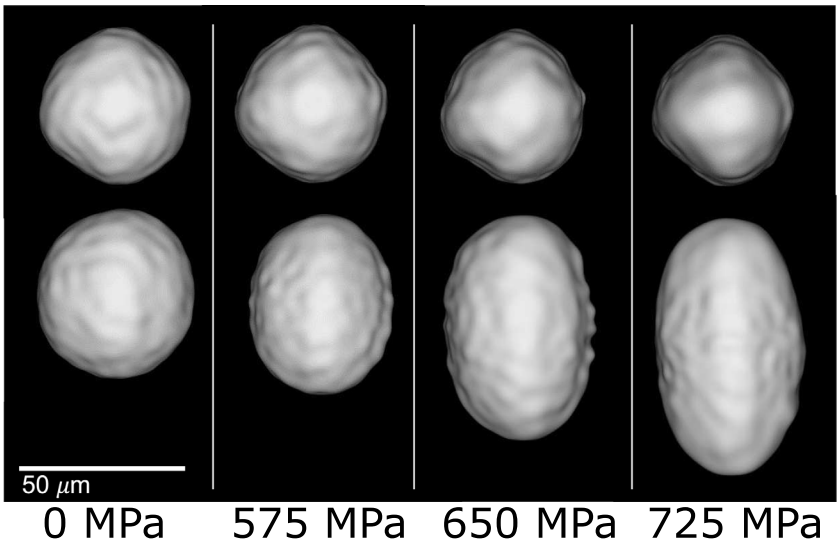

Fig. 15. The large pore in H2-4, extending in the loading direction, before it moves out of the field of view. The prominent pore can be seen in context in Fig. 13(1) when at 575 MPa, visualized as smoothed renderings. Top row — looking down on the pore in the negative z-direction (into page). Bottom row — looking in the negative y-direction, z-direction is up, toward the top of the page.

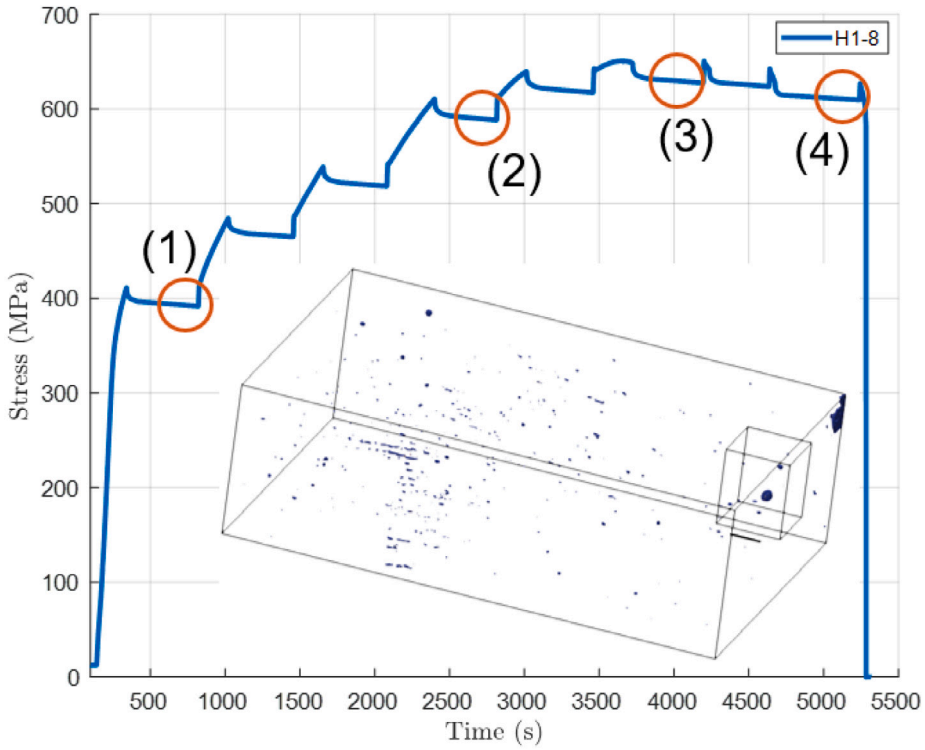

Fig. 16. Stress versus time (which shows the hold periods), with the circled points showing stress values at which the single-pore deformation images shown in Fig. 17 were taken. The single-pore deformation region in Fig. 17 is a sub-volume of the larger image, highlighted by the smaller boxed region in the inset image.

5. Crystal plasticity modeling of anisotropic pore evolution

The measurement of pore deformation shown here provides an opportunity to directly compare finite deformation microstructure-based modeling of pore deformation with experimental measurements. This provides increased confidence in the microscale models, if the overall shape of the pore can be reproduced computationally when calibrating the model with overall stress–strain data. The anisotropic pore deformation captured by the experiments motivates using a crystal plasticity (CP) material law, derived from the work of McGinty (McGinty, 2001).

Crystallographic measurements (Appendix A) show that the grains in this materials are on the order of 2 mm tall (in the build direction) and 0.2 mm wide, i.e. much larger than the pores. So it is reasonable to assume that a pore is entirely surrounded by a single crystal. Thus, we build our model with a single crystal unit cell of 65 μm × 65 μm × 65 μm embedded with a relatively large pore. The pore itself was extracted directly from the XCT images (Fig. 19), and thus the initial shape of the pore is identical in experiment and simulation.

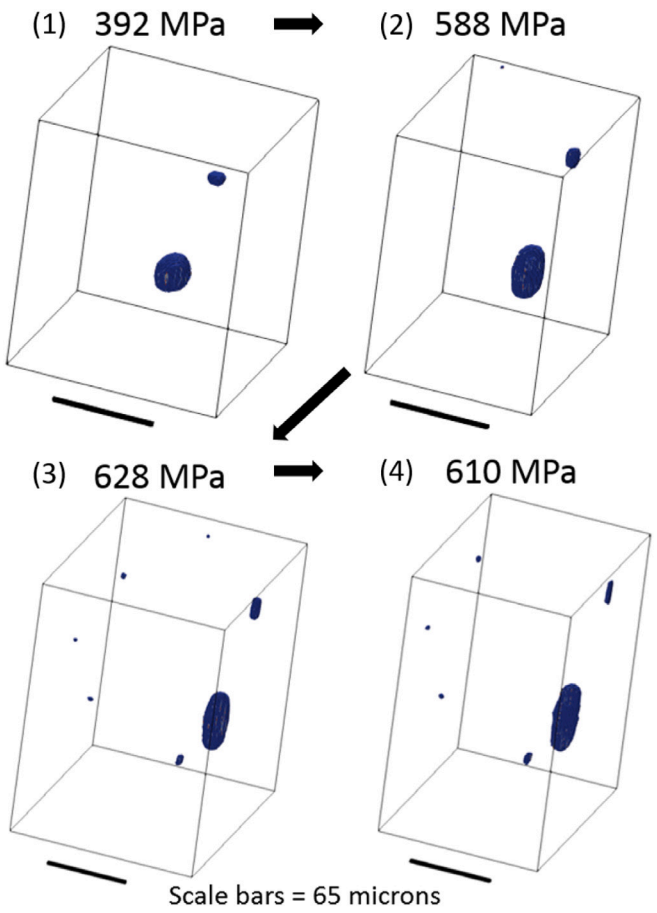

Fig. 17. Images of a single, large pore deforming in specimen H1-8, along with the overall engineering stress state at which the respective images were taken; the pore elongates along the loading direction and new pores (either grown above the observation threshold, newly nucleated, or moved into the field of view) appear.

The assumption of a single crystal surrounding the pore also provides a means with which to conduct inverse modeling: the crystallographic orientation surrounding pore predominantly impacts the orientation of maximal and minimal contraction of the pore during deformation, and this local information can be used to identify grain orientation (as a model input) while keeping all calibration parameters constant. Although with the current dataset we are unable to validate the orientation prediction, we can at least demonstrate this kind of potential usage for coupled simulation–experimental investigations, with the hope it could be proven useful in future investigations.

Details of the CP material model implementation are provided in Appendix D. The CP material model was implemented in a reduced order modeling method called Crystal Plasticity Self-consistent Clustering Analysis (CPSCA) (Yu et al., 2019; Liu et al., 2018). The finite deformation implementation of CPSCA used for this work is explained in detail in Yu (2019). The material parameters, given in Table 4, are used to approximately match the average stress–strain curves. Currently, the elastic properties are isotropic, not anisotropic, which had little impact upon the overall results.

With these parameters calibrated, the remaining question is: what grain orientation led to the specific pore deformation observed in the experiment? To answer this question, an optimization algorithm is used to iteratively find the grain orientation by minimizing the difference between the predicted pore shape and measured pore shape, using of a fast numerical model. This process only changed the input grain orientation, none of the calibration parameters.

Table 4
Crystal plasticity parameters, those marked with a dagger symbol were taken directly from Cruzado et al. (2017). The remainder were calibrated with the thin wall tensile test data.

C_{11} (GPa)	C_{12} (GPa)	C_{44} (GPa)	
196.40	84.17	56.12	
$\dot{\gamma}_0^{\alpha}$ (s^{-1})	$\tilde{m}$	$\tau_0^{\alpha,t=0}$ (MPa)	$a^{\alpha,t=0}$ (MPa)
$2.42 \times 10^{-3\dagger}$	$58.8^{\dagger}$	171.85	0.0
H (MPa)	R (MPa)	h (MPa)	r (MPa)
1.0	0.0	500.0	0.0

5.1. Overall CPSCA pore shape predictions

Because the pore is in a single crystal, preferential deformation in one orientation occurs driving the initially sphere-like defect to a three-axis ellipsoid. The overall shape of the pore throughout the load steps matches between the prediction of the simulation and the measurement of the experiment. By changing the orientation of the crystal in the model, the observed axes of minimal and maximal contraction can be reproduced. Other than the orientation of the maximal and minimal constrictions, the overall shape prediction is independent of the inverse model described above. Although only shown for one case, the high quality of the match provide some confidence in the ability of our CP method to reproduce the local deformation of micro-scale pores in DED IN718, but further validation would be beneficial. A comparison of two projections (top-down and side-on) of the pore as measured and as modeled are shown in Fig. 20. In both simulation and experiment, the pore extends in the load direction as shown in the side projection in the top two rows of Fig. 20. The pore predominately contracts in the 45° direction in the x–y plane while hardly contracting at all in the 135° direction in the x–y plane, as shown in the top-down projection in the second two rows of Fig. 20. These deformations result are from a crystal with lattice orientation (45°, 45°, 0°). Only the input parameter of grain orientation was changed, the calibration parameters were unmodified, to identify the grain orientation that resulted in a good match in deformation. Thus, we suppose that (a) the initial calibration could produce the given void deformation as a pure prediction, given grain orientation information (unavailable with the current experiment); and (b) that the grain orientation can be computed using an inverse approach and CP model calibrated to average stress–strain properties.

6. Summary, conclusions, and future work

6.1. Summary and conclusions

This work presented a series of pore and mechanical characterizations of thin-wall IN718 samples produced using DED, and tested with *in-situ* techniques to track pores during mechanical testing. Largely 3D measurements showed the complex, heterogeneous, and anisotropic nature of the material. Mechanical testing alongside 3D measurements of pores provided unique insight into the deformation behavior of the material in ways that would not be possible to understand without *in-situ* monitoring of deformation. In summary:

- Material properties vary significantly from location to location, with orientation, and with processing condition. Orientation variability is in keeping with prior published results for similar material. Although a wide spread was observed in our tests, the general trends indicated that horizontally oriented specimens have similar higher elastic modulus, yield and ultimate stress at the deficit of elongation when compared with vertically oriented specimens.
- We hypothesize that location-to-location differences are related to thermal difference in the build; although differences in porosity exist, at the scales of pores observed, they seem to have little impact on the progression of plastic deformation, necking, and ductile damage.

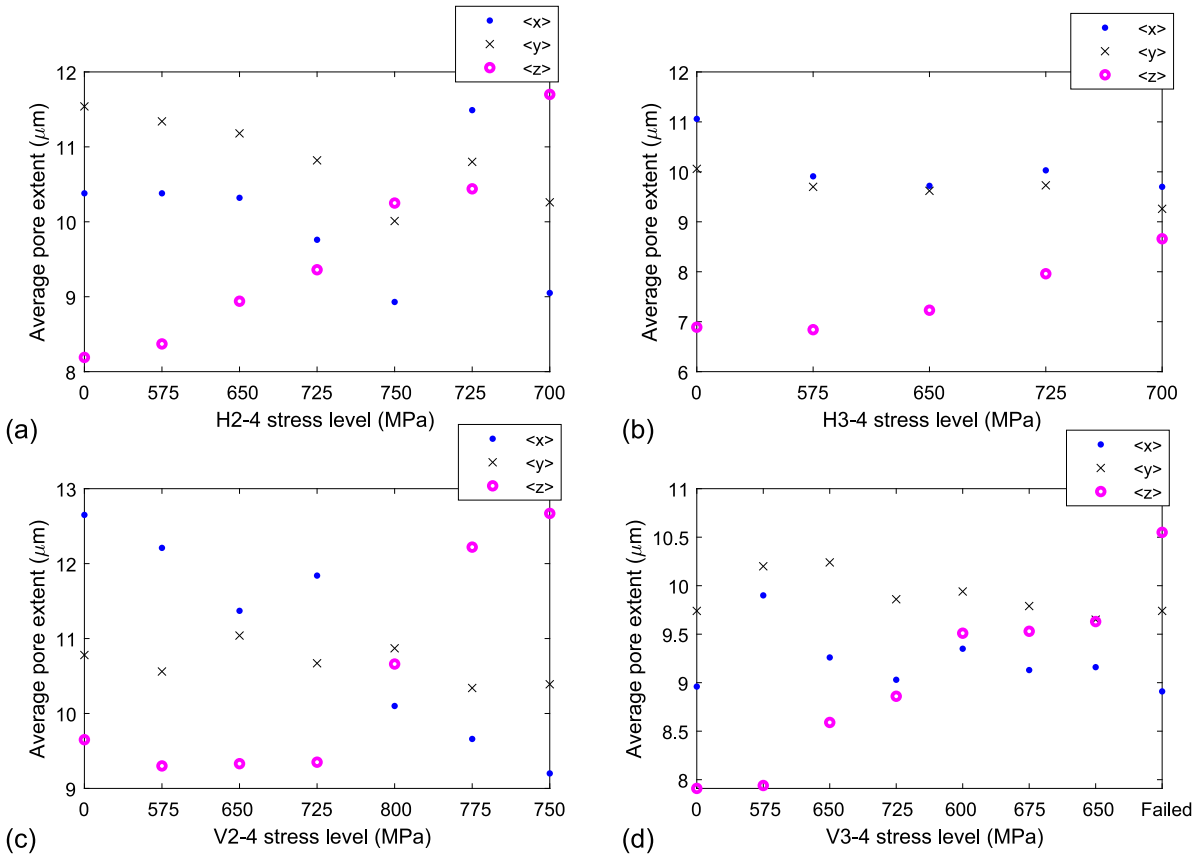

Fig. 18. Pore extents (in μm) averaged across all pores in each subsequent XCT image during loading, for specimens: (a) H2-4, (b) H3-4, (c) V2-4, (d) V3-4.

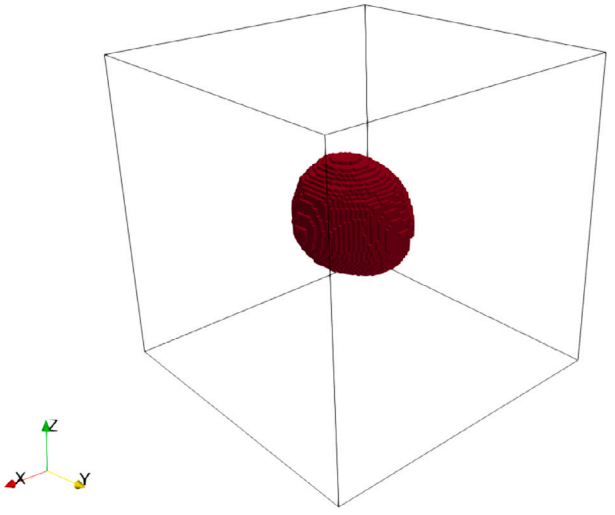

Fig. 19. A single crystal unit cell of 65 μm × 65 μm × 65 μm embedded with a big pore (in red).

- The wall with 60 s dwell time seems to generally undergo large deformation before failure; prior work also indicates that local thermal condition difference lead to quantifiable differences in UTS, Bennett et al. (2018), although this was not directly studied in the current work.
- Pore deformation has been measured:
  - For this process and material, pores are on the sub-grain scale (grains are relatively large compared to pores); for the larger pores specifically studied, pore volume tends to increase slightly as deformation level increases.
  - Pores tend to elongate with the material during deformation.
  - Greater pore shape change appears to correlate with greater maximum elongation, i.e., the build with 60 s dwell (wall 2) tended to undergo more elongation and greater shape change than those in the walls without a dwell time.
  - In most cases, these failures do not seem strongly defect-driven and ductile deformation develops despite a general dispersion of small, generally spherical pores. We conclude that for ligaments on the 1 mm-edge-length scale such as our test specimens, pores with average size roughly 10 μm are not dominating the plastic response.
- A crystal plasticity material model implemented in the CPSCA reduced order scheme was used to simulate the pore shape change of a specific, large pore.
- Although not validated, one potential implication of the CP-SCA modeling is that grain orientation might be inferred from preferential single-crystal deformation patterns

These conclusions are general restricted to similar material, i.e. high-density IN718 with small, semi-randomly distributed, roughly spherical pores. Only highlights of the complete data set obtained have been shown, along with aggregated data. Full testing to construct the average stress–strain curves included some 74 in-situ tests. This full data set represents a rich corpus of evidence that could be further explored in several different ways in future work.

The full data set, including stress–strain data (and curves), selected XCT data, and Matlab processing scripts are provided, archived and

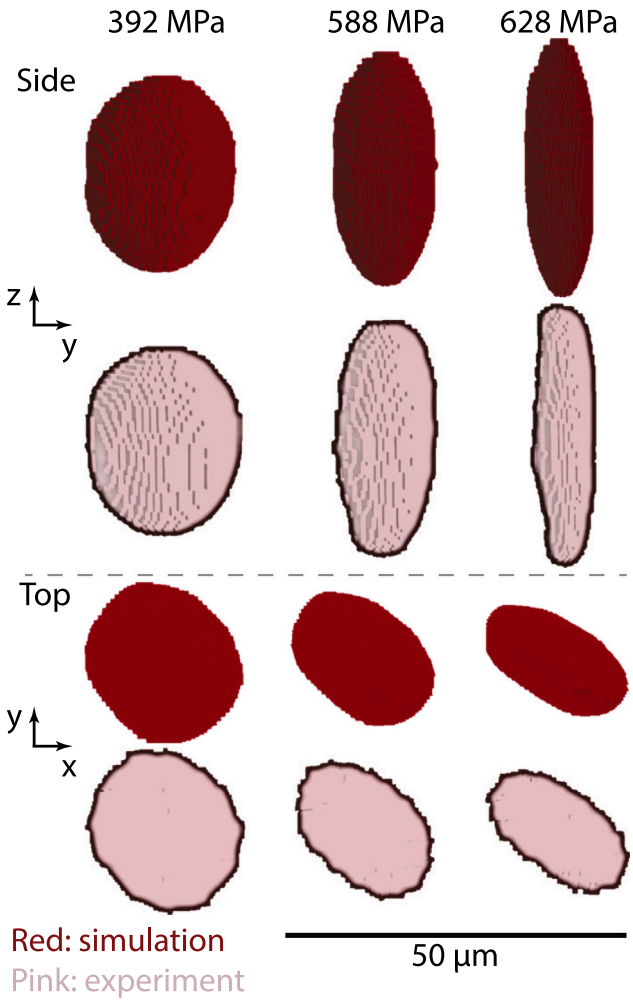

Fig. 20. A single pore deforming in a single crystal. The two rows show "side" and "top" views, with each sub-row showing the comparison of measurement (red) and model (pink) at different stress levels. The model predicts well the deformation patterns observed in the experiment using macroscopically calibrated model parameters and a lattice orientation of (45°, 45°, 0°).

publicly accessible by DOI on NIST's MIDAS data service (URL/DOI to be added). Interested readers, and those curious enough to pursue future work with the data are encouraged to contact us and download the publicly available dataset.

6.2. Possible future work

In order to make the most use of the *in-situ* testing, digital volume correlation (DVC) or a similar technique, could be used to reconstruct 3D strain fields in the measured volume. This would allow for even more direct comparison between models and experiments. It would also provide a deeper insight into the deformation behaviors of the material. However, because the only contrast available currently in these specimens is the pores themselves, it is unlikely that information on the pore scale or in between pores could be reliably obtained with the current data.

Further it is well known that localized deformation (necking) will change the stress triaxiality within the area-reduction region. Since stress triaxiality is a controlling factor in damage and fracture, a future study focused on post-localization deformation and fracture behavior could use this data to compute area reduction, ductility, and localize triaxiality changes; computation of the triaxiality from these images would be relatively easy. The addition of optical or electron microscopy fractography or other post-failure analysis would be of interest to more thoroughly quantify the failure behavior and any potential differences in failure behavior between build conditions and conventionally processed IN718.

Further analysis of microstructure features other than pores could be conducted. Study of the reduction of area versus elongation would provide a quantifiable measure for ductility. Measurement of final cross section could be done on either the specimens themselves, or using reconstructed XCT scans of the fracture regions (Supplemental Information 3 provides an example of the XCT scans of fracture regions). Noisy thermal measurements made during the build make it difficult to quantify the thermal conditions and thus difficult to relate those to specific specimens and their behavior. However, it has been possible to compare ultimate tensile strength to thermal indicators for these specimens (Bennett et al., 2018), and future analysis could include more thorough comparisons between measured mechanical performance indicators (e.g. stiffness, ultimate strength, yield strength, elongation) and spatial location or thermal history for the various different coupons and walls. Another recent study on the same material found a correlation between solidification cooling rate and pore size (Kafka et al., 2021), and further correlations between thermal indicators and critical features for modeling would be advantageous to discover.

Another aspect that could be further studied is the systematization of inverse modeling to identify grain orientation on the basis of pore deformation. In theory, such a model could be used to provide grain orientation maps, where orientation is known in the local vicinity of an observed pore. While computationally somewhat expensive, this would provide additional information to XCT-only experiments (i.e. no diffraction data is collected) with little or no additional experimental effort. This would enrich the kind of data that can be collected, in 3D, on tomographic equipment, possibly even on laboratory-scale *in-situ* XCT equipment.

CRediT authorship contribution statement

Orion L. Kafka: Conceptualization, Methodology, Software, Validation, Investigation, Resources, Data curation, Writing – original draft, Writing – review & editing, Project administration, Visualization, Supervision, Funding acquisition. **Cheng Yu:** Conceptualization, Methodology, Software, Validation, Investigation, Writing – review & editing, Visualization, Funding acquisition. **Puikei Cheng:** Conceptualization, Methodology, Investigation, Writing – review & editing, Project administration, Funding acquisition. **Sarah J. Wolff:** Conceptualization, Methodology, Investigation, Resources, Writing – review & editing, Project administration, Funding acquisition. **Jennifer L. Bennett:** Conceptualization, Methodology, Investigation, Writing – review & editing. **Edward J. Garboczi:** Investigation, Software, Supervision, Writing – review & editing. **Jian Cao:** Resources, Funding acquisition, Writing – review & editing. **Xianghui Xiao:** Conceptualization, Methodology, Software, Resources, Writing – review & editing. **Wing Kam Liu:** Resources, Supervision, Funding acquisition, Writing – review & editing.

Declaration of competing interest

The authors declare that they have no known competing financial interests or personal relationships that could have appeared to influence the work reported in this paper.

Data availability

All the data is provided in an associated data publication, which is referenced by DOI in the references section and hosted on the NIST Public Data Repository.

Acknowledgments

This work made use of the MatCI Facility which receives support from the MRSEC Program (National Science Foundation DMR-1720139) of the Materials Research Center at Northwestern University. We specifically thank Carla Shute at the MatCI facility for her advice during specimen preparation. Specimens were fabricated using funding from DMDII grant number 15-07-07; OLK, CY, and WKL thank the National Science Foundation for support under grants CMMI-1762035 and CMMI-1934367. Part of this research was conducted while OLK held a National Research Council Postdoctoral Research Associateship at the National Institute of Standards and Technology. We gratefully acknowledge the help of J.-S. Park of APS Beamline 1ID, who provided the mini-tensile load frame used throughout the work, as well as technical support for the load frame and helpful suggestions for the research.

Appendix A. Crystallography

The microstructure consisting of large columnar grains with high aspect ratio and a preferred crystallographic orientation seems most prevalent, although a relatively small area was sampled. Micro-Laue diffraction at APS beamline 34-ID-E was conducted on a small region cut from the top corner of the thin wall, and Fig. A.21 shows two dominant features from these measurements: first, similar elongated grains with a predominately orientated in between the (101) and (001) directions is seen; second, the final layer of the build exhibits a unique orientation, mostly (111), likely due to the lack of re-solidification during processing of that layer (however, the this is supposition based on prior reports (Zhang et al., 2020) and direct evidence, for example from *in-situ* measurements, of this mechanism has not been demonstrated to our knowledge). The existence of large, columnar, preferentially oriented grains near where the test specimen were extracted from was corroborated with electron backscatter diffraction (EBSD) measurements (not shown; available upon request).

Appendix B. Detailed horizontal vs vertical data

Fig. B.22(a–c) shows a similar comparison for Young's modulus between the vertical and horizontal specimens for each processing condition. Fig. B.23(a–c) compares the 0.2% offset yield stresses. Fig. B.24(a–c) shows the ultimate tensile strengths, and Fig. B.25(a–c) shows a comparison of the elongation at failure (determined from the DIC data) within each wall for both vertical and horizontal specimens. All sets of box-and-whisker plots match the average trends observed in Fig. 10, but provide more quantification of the specific values often used in

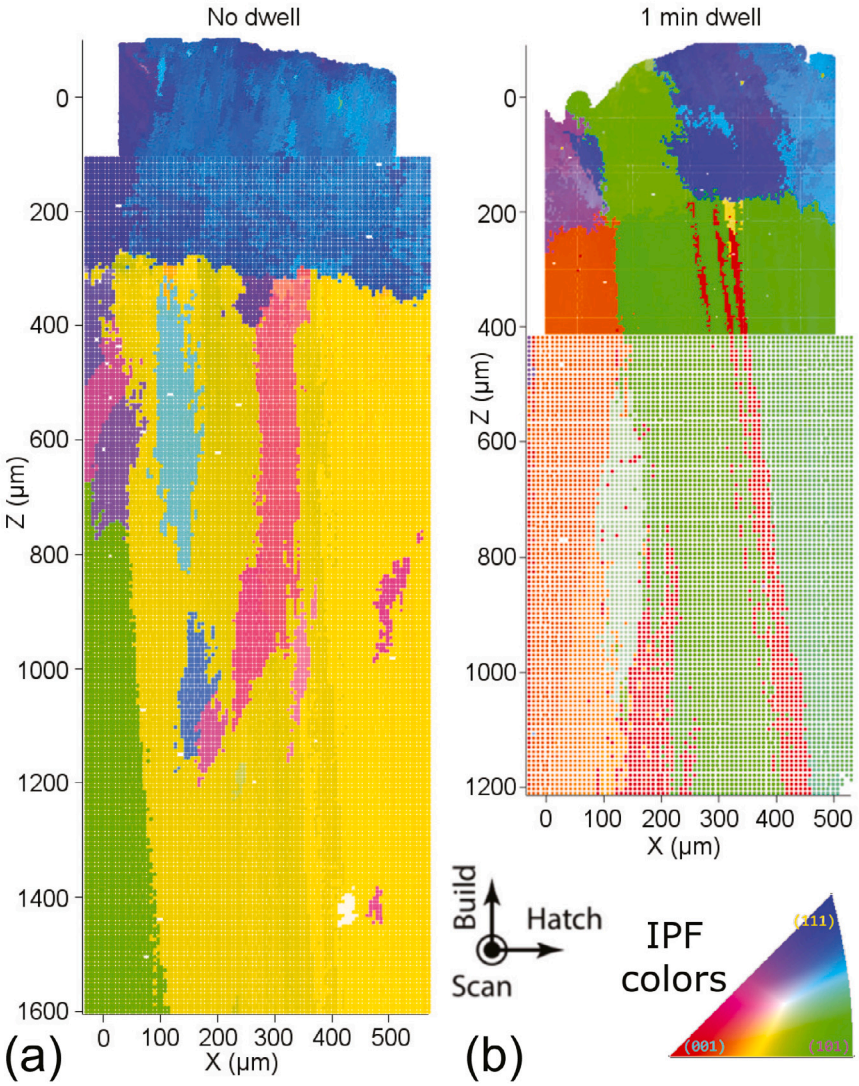

Fig. A.21. X-ray micro-Laue diffraction (conducted at APS beamline 34-ID-E) images of the top corner of the no-dwell and one-minute dwell builds. Colored according to the IPF diagram. The apparent "grid" is a result of the visualization chosen to represent finite probe size during point-scanning.

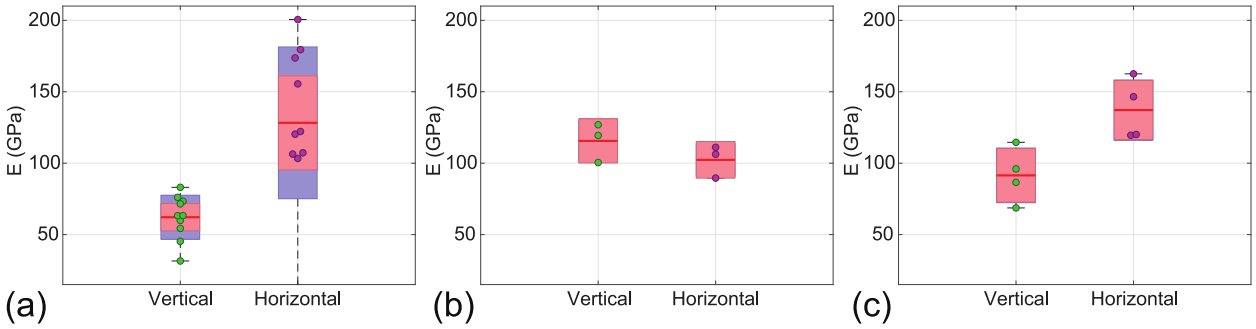

Fig. B.22. Box-and-whisker plots showing the mean (red line), standard deviation (salmon region), 95% confidence interval (blue region), and extents (whiskers) of elastic modulus for (a) processing condition 1, (b) processing condition 2, (c) processing condition 3. Because modulus was measured before any of the stops, these all can be compared fairly. Individual green (vertical) or magenta (horizontal) points indicate individual tests (the points are moved slightly in the x-axis to be individually identifiable).

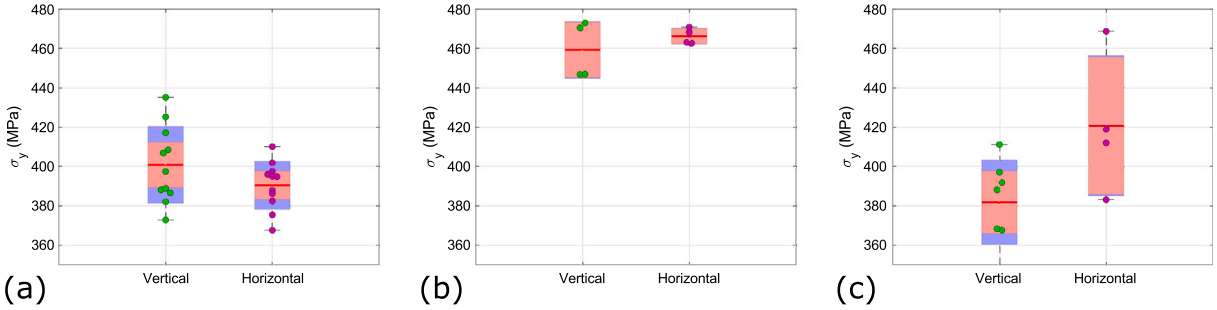

Fig. B.23. Box-and-whisker plot showing the spread and mean values for yield stress for (a) processing condition 1, (b) processing condition 2, and (c) processing condition 3; in most cases, yield occurs before the first scan, so continuous and interrupted tests are generally comparable.

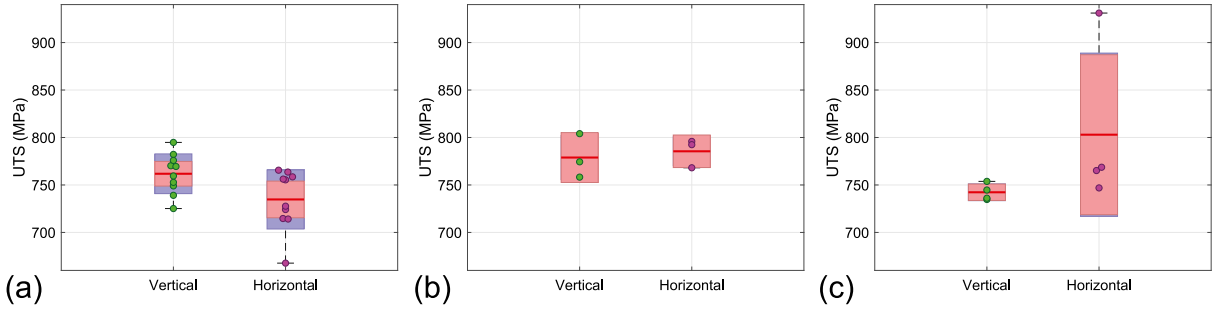

Fig. B.24. A similar plot to Fig. B.25, this time showing ultimate tensile strength for (a) processing condition 1, (b) processing condition 2, (c) processing condition 3. A mix of continuous and interrupted loading may make this comparison less reliable when comparing wall 1 (a) to walls 2 (b) and 3 (c).

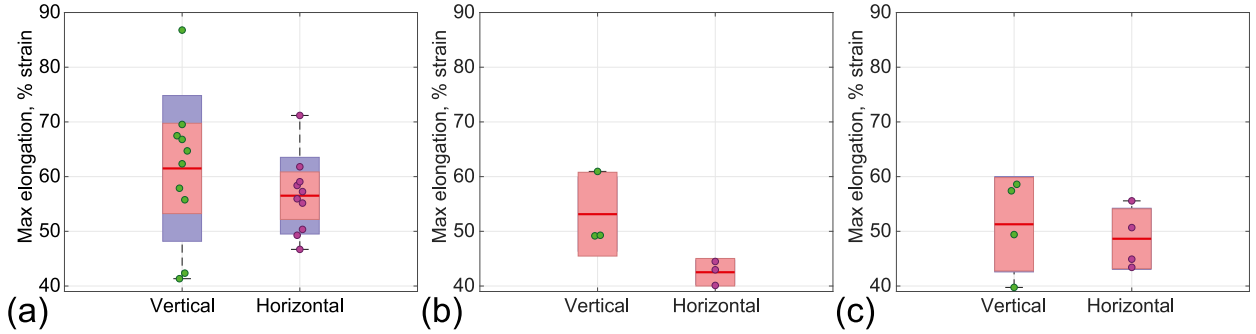

Fig. B.25. Box-and-whisker plot showing maximum elongation for each specimen for (a) wall 1, (b) wall 2, (c) wall 3. Note that only walls 2 and 3 are necessarily directly comparable, because both are based on interrupted (stop–start) testing, whereas wall 1 was not.

engineering design. In each figure, the red line is the mean value, each dot represents an individual specimen, the salmon colored region represents one standard deviation (SD), the blue region represents a 95% confidence interval (CI), and the outliers are plotted on the

Table C.5
H2-4 average pore data, all lengths in μm.

Stress level (MPa)	0	575	650	725	750	725	700
# pores	111	84	83	93	106	82	80
<L>n	12.19	12.07	12.05	12.24	12.22	14.13	13.7
<W>n	10.36	10.56	10.76	10.35	9.94	11.12	10.1
<T>n	8.41	8.44	8.68	8.54	7.85	7.82	7.5
<L/T>	1.54	1.52	1.45	1.51	1.57	2.00	1.83
<x>	10.38	10.38	10.32	9.76	8.93	11.49	9.05
σ_x	3.08	2.77	2.72	3.17	2.7	3.62	3.59
<y>	11.54	11.34	11.18	10.82	10.01	10.80	10.26
σ_y	3.42	3.37	3.31	3.18	2.75	3.48	3.67
<z>	8.19	8.37	8.94	9.36	10.25	10.44	11.7
σ_z	3.27	3.89	4.55	4.64	4.34	5.41	6.15

Table C.6
H3-4 average pore data, all lengths in μm.

Stress level (MPa)	0	575	650	725	700
# pores	274	311	301	245	267
<L>n	12.64	11.58	11.58	12.13	12.14
<W>n	9.10	8.67	8.63	8.99	8.79
<T>n	6.25	6.48	6.63	6.92	6.88
<L/T>	2.16	1.93	1.87	1.84	1.83
<x>	11.06	9.91	9.72	10.03	9.70
σ_x	3.57	2.99	2.88	2.97	2.97
<y>	10.06	9.70	9.62	9.73	9.26
σ_y	2.32	2.31	2.39	2.69	2.29
<z>	6.89	6.84	7.23	7.96	8.66
σ_z	3.01	2.98	3.24	3.39	3.7

Table C.7
V2-4 average pore data, all lengths in μm.

Stress level (MPa)	0	575	650	725	800	775	750
# pores	391	175	183	190	102	128	103
<L>n	14.73	14.02	13.56	13.94	13.07	14.15	14.31
<W>n	10.63	10.72	10.39	10.43	10.61	10.39	10.23
<T>n	7.91	8.00	8.31	8.01	8.75	8.39	8.18
<L/T>	1.93	1.89	1.71	1.87	1.5	1.66	1.7
<x>	12.65	12.21	11.37	11.84	10.1	9.66	9.20
σ_x	4.62	4.71	4.3	4.16	3.34	2.94	2.82
<y>	10.78	10.56	11.04	10.67	10.87	10.34	10.39
σ_y	3.12	3.39	3.14	2.86	3.07	3.27	3.1
<z>	9.65	9.30	9.33	9.35	10.66	12.22	12.67
σ_z	4.52	4.56	4.32	4.64	5.92	7.28	7.55

Table C.8
V3-4 average pore data, all lengths are in μm.

Stress level (MPa)	0	575	650	725	600	675	650	Failed
# pores	236	159	164	164	158	159	163	182
<L>n	11.52	12.15	12.08	11.86	12.41	12.32	12.40	13.01
<W>n	8.62	9.16	9.20	9.19	9.55	9.36	9.35	9.36
<T>n	7.00	7.34	7.36	7.46	7.52	7.42	7.33	7.16
<L/T>	1.73	1.88	1.73	1.65	1.7	1.73	1.81	1.86
<x>	8.96	9.90	9.26	9.03	9.35	9.13	9.16	8.91
σ_x	3.07	4.74	3.9	2.88	3.83	3.76	3.49	3.35
<y>	9.74	10.20	10.24	9.86	9.94	9.79	9.65	9.74
σ_y	2.37	3.4	3.31	2.75	3.28	3.16	2.69	2.82
<z>	7.91	7.94	8.59	8.86	9.51	9.53	9.63	10.55
σ_z	2.61	3.21	3.4	3.81	4.85	4.65	4.82	4.97

whiskers. Note that these values (SD and CI) are intended for data that are normally distributed, but this is not necessarily true here because spatial variability is likely driven by non-random thermal conditions.

Appendix C. Detailed average pore deformation tables

Tabular data detailing all computed void descriptive measures averaged across all pores observed in each image. The notation $\langle\boxdot\rangle$ n indicates the number average of parameter $\boxdot$, and $\sigma_{x,y,z}$ indicates first standard deviation of the extents x, y, and z.

Appendix D. Crystal plasticity modeling method

In this computational crystal plasticity implementation, the local deformation gradient $\mathbf{F}$ is multiplicatively decomposed into elastic $\mathbf{F}^{\mathrm{e}}$ and inelastic $\mathbf{F}^{\mathrm{in}}$ contributions:

$$\mathbf{F} = \mathbf{F}^{\mathrm{e}} \cdot \mathbf{F}^{\mathrm{in}}. \tag{D.1}$$

The inelastic deformation gradient $\mathbf{F}^{\mathrm{in}}$ can be determined using a plastic constitutive law to relate the plastic velocity gradient $\mathbf{L}^{\mathrm{p}} = \dot{\mathbf{F}}^{\mathrm{p}} \cdot \left(\mathbf{F}^{\mathrm{p}}\right)^{-1}$ to the plastic shear rate $\dot{\gamma}^{\alpha}$ across all slip systems $1 \ldots \alpha$ through

$$\mathbf{L}^{\mathrm{p}} = \sum_{\alpha=1}^{N_{\mathrm{slip}}} \dot{\gamma}^{\alpha} (\mathbf{s}_0^{\alpha} \otimes \mathbf{n}_0^{\alpha}). \tag{D.2}$$

Here, $\mathbf{s}_0^{\alpha}$ and $\mathbf{n}_0^{\alpha}$ are unit vectors that define the slip direction and slip plane normal for slip system α in the undeformed configuration, N_{slip} is the number of active slip systems, and $\otimes$ is the dyadic product. In general, the plastic shear rate $\dot{\gamma}^{\alpha}$ in slip system α is taken to be a function of resolved shear stress τ^{α}, deformation resistance τ_0^{α}, and back stress a^{α} in that slip system. The resolved shear stress is given by

$$\tau^{(\alpha)} = \boldsymbol{\sigma} : (\mathbf{s}^{\alpha} \otimes \mathbf{n}^{\alpha}), \tag{D.3}$$

where $\boldsymbol{\sigma}$ is the Cauchy stress, $\mathbf{s}^{(\alpha)}$ is the slip direction, and $\mathbf{n}^{(\alpha)}$ is the slip plane normal, all of which are defined in the deformed configuration. They are computed from their counterparts in the undeformed configuration with

$$\begin{cases} \boldsymbol{\sigma} = \frac{1}{J_e}\left[\mathbf{F}^{e} \cdot \mathbf{S}^{e} \cdot (\mathbf{F}^{e})^{\mathrm{T}}\right], \\ \mathbf{s}^{\alpha} = \mathbf{F}^{e} \cdot \mathbf{s}_0^{\alpha}, \\ \mathbf{n}^{\alpha} = \mathbf{n}_0^{\alpha} \cdot (\mathbf{F}^{e})^{-1}. \end{cases} \tag{D.4}$$

The evolution law for γ^{α} is given by

$$\dot{\gamma}^{\alpha} = \dot{\gamma}_0 \left| \frac{\tau^{\alpha} - a^{\alpha}}{\tau_0^{\alpha}} \right|^{(\tilde{m}-1)} \left(\frac{\tau^{\alpha} - a^{\alpha}}{\tau_0^{\alpha}} \right), \tag{D.5}$$

where $\dot{\gamma}_0$ is a reference shear rate, and $\tilde{m}$ is the exponent related to material strain rate sensitivity. The evolution laws for deformation resistance τ_0^{α} (the isotropic hardening term) and back stress a^{α} (the kinematic hardening term) are given by McGinty (McGinty, 2001):

$$\begin{cases} \dot{\tau}_0^{\alpha} = H \sum_{\beta=1}^{N_{\mathrm{slip}}} |\dot{\gamma}^{\beta}| - R\tau_0^{\alpha} \sum_{\beta=1}^{N_{\mathrm{slip}}} |\dot{\gamma}^{\beta}|, \\ \dot{a}^{\alpha} = h\dot{\gamma}^{\alpha} - ra|\dot{\gamma}^{\alpha}| \end{cases} \tag{D.6}$$

where H and h are direct hardening coefficients, and R and r are dynamic recovery coefficients. Note that in Eq. (D.6) we assume the latent hardening and self-hardening effects are identical.

Appendix E. Supplementary data

Supplementary material related to this article can be found online at https://doi.org/10.1016/j.ijsolstr.2022.111943.

References

Anderson, M., Thielin, A.-L., Bridier, F., Bocher, P., Savoie, J., 2017. δ Phase precipitation in Inconel 718 and associated mechanical properties. Mater. Sci. Eng. A 679, 48–55. http://dx.doi.org/10.1016/j.msea.2016.09.114.

Bain, E.D., Garboczi, E.J., Seppala, J.E., Parker, T.C., Migler, K.B., 2019. AMB2018-04: Benchmark physical property measurements for powder bed fusion additive manufacturing of polyamide 12. Integr. Mater. Manuf. Innov. 8 (3), 335–361. http://dx.doi.org/10.1007/s40192-019-00146-3.

Bennett, J., Glerum, J., Cao, J., 2021. Relating additively manufactured part tensile properties to thermal metrics. CIRP Ann. 70 (1), 187–190. http://dx.doi.org/10.1016/j.cirp.2021.04.053.

Bennett, J.L., Kafka, O.L., Liao, H., Wolff, S.J., Yu, C., Cheng, P., Hyatt, G., Ehmann, K., Cao, J., 2018. Cooling rate effect on tensile strength of laser deposited Inconel 718. In: Procedia Manuf., Vol. 26. pp. 912–919. http://dx.doi.org/10.1016/j.promfg.2018.07.118.

Bennett, J.L., Wolff, S.J., Hyatt, G., Ehmann, K., Cao, J., 2017. Thermal effect on clad dimension for laser deposited Inconel 718. J. Manuf. Process. 28, 550–557. http://dx.doi.org/10.1016/j.jmapro.2017.04.024.

Benzing, J.T., Liew, L.A., Hrabe, N., DelRio, F.W., 2020. Tracking defects and microstructural heterogeneities in meso-scale tensile specimens excised from additively manufactured parts. Exp. Mech. 60 (2), 165–170. http://dx.doi.org/10.1007/s11340-019-00558-4.

Bigger, R., Blaysat, B., Boo, C., Grewer, M., Hu, J., Jones, A., Klein, M., Raghavan, K., Reu, P., Schmidt, T., Siebert, T., Simenson, M., Turner, D., Vieira, A., Weikert, T., 2018. A good practices guide for digital image correlation. Int. Digital Image Correl. Soc. 94. http://dx.doi.org/10.32720/idics/gpg.ed1.

Blackwell, P., 2005. The mechanical and microstructural characteristics of laser-deposited IN718. J. Mater Process. Technol. 170 (1), 240–246. http://dx.doi.org/10.1016/j.jmatprotec.2005.05.005.

Burhenne, S., Jacob, D., Henze, G.P., 2011. Sampling based on Sobol sequences for Monte Carlo techniques applied to building simulations. In: Proceedings of Building Simulation 2011: 12th Conference of International Building Performance Simulation Association. pp. 1816–1823.

Carlton, H.D., Haboub, A., Gallegos, G.F., Parkinson, D.Y., MacDowell, A.A., 2016. Damage evolution and failure mechanisms in additively manufactured stainless steel. Mater. Sci. Eng. A 651, 406–414. http://dx.doi.org/10.1016/j.msea.2015.10.073.

Cruzado, A., LLorca, J., Segurado, J., 2017. Modeling cyclic deformation of Inconel 718 superalloy by means of crystal plasticity and computational homogenization. Int. J. Solids Struct. 122, 148–161.

du Plessis, A., Yadroitsava, I., Yadroitsev, I., 2020. Effects of defects on mechanical properties in metal additive manufacturing: A review focusing on X-ray tomography insights. Mater. Des. 187, 108385. http://dx.doi.org/10.1016/j.matdes.2019.108385.

Efstathiou, C., Boyce, D., Park, J.-S., Lienert, U., Dawson, P., Miller, M., 2010. A method for measuring single-crystal elastic moduli using high-energy X-ray diffraction and a crystal-based finite element model. Acta Mater. 58 (17), 5806–5819. http://dx.doi.org/10.1016/j.actamat.2010.06.056.

Gan, Z., Li, H., Wolff, S.J., Bennett, J.L., Hyatt, G., Wagner, G.J., Cao, J., Liu, W.K., 2019. Data-driven microstructure and microhardness design in additive manufacturing using a self-organizing map. Engineering 5 (4), 730–735. http://dx.doi.org/10.1016/j.eng.2019.03.014.

Garboczi, E.J., Hrabe, N., 2020a. Particle shape and size analysis for metal powders used for additive manufacturing: Technique description and application to two gas-atomized and plasma-atomized Ti64 powders. Addit. Manuf. 31, 100965. http://dx.doi.org/10.1016/j.addma.2019.100965.

Garboczi, E.J., Hrabe, N., 2020b. Three-dimensional particle shape analysis using X-ray computed tomography: Experimental procedure and analysis algorithms for metal powders.. J. Vis. Exp. (166), http://dx.doi.org/10.3791/61636.

Glerum, J., Bennett, J., Ehmann, K., Cao, J., 2021. Mechanical properties of hybrid additively manufactured Inconel 718 parts created via thermal control after secondary treatment processes. J. Mater Process. Technol. 291, 117047. http://dx.doi.org/10.1016/j.jmatprotec.2021.117047.

Gordon, J., Vinci, R., Hochhalter, J., Rollett, A., Harlow, D.G., 2019. Quantification of location-dependence in a large-scale additively manufactured build through experiments and micromechanical modeling. Materialia 7, 100397. http://dx.doi.org/10.1016/j.mtla.2019.100397.

Gorelik, M., 2017. Additive manufacturing in the context of structural integrity. Int. J. Fatigue 94, 168–177. http://dx.doi.org/10.1016/j.ijfatigue.2016.07.005.

Guévenoux, C., Hallais, S., Charles, A., Charkaluk, E., Constantinescu, A., 2020. Influence of interlayer dwell time on the microstructure of Inconel 718 laser cladded components. Opt. Laser Technol. 128, 106218. http://dx.doi.org/10.1016/j.optlastec.2020.106218.

Gürsoy, D.D., De Carlo, F., Xiao, X., Jacobsen, C., 2014. TomoPy: a framework for the analysis of synchrotron tomographic data. J. Synchrotron Radiat. 21 (5), 1188–1193. http://dx.doi.org/10.1107/S1600577514013939.

Hastie, J.C., Koelblin, J., Kartal, M.E., Attallah, M.M., Martinez, R., 2021. Evolution of internal pores within AlSi10Mg manufactured by laser powder bed fusion under tension: As-built and heat treated conditions. Mater. Des. 204, 109645. http://dx.doi.org/10.1016/j.matdes.2021.109645.

Herroitt, C., Li, X., Kouraytem, N., Tari, V., Tan, W., Anglin, B., Rollett, A., Spear, A., 2019. A multi-scale, multi-physics modeling framework to predict spatial variation of properties in additive-manufactured metals. Model. Simul. Mater. Sci. Eng. 27 (2), 025009. http://dx.doi.org/10.1088/1361-651x/aaf753.

Hosseini, E., Popovich, V., 2019. A review of mechanical properties of additively manufactured Inconel 718. Addit. Manuf. 30, 100877. http://dx.doi.org/10.1016/j.addma.2019.100877.

Jinoop, A., Paul, C., Mishra, S., Bindra, K., 2019. Laser additive manufacturing using directed energy deposition of Inconel-718 wall structures with tailored characteristics. Vacuum 166, 270–278. http://dx.doi.org/10.1016/j.vacuum.2019.05.027.

Kafka, O.L., Jones, K.K., Yu, C., Cheng, P., Liu, W.K., 2021. Image-based multiscale modeling with spatially varying microstructures from experiments: Demonstration with additively manufactured metal in fatigue and fracture. J. Mech. Phys. Solids 150, http://dx.doi.org/10.1016/j.jmps.2021.104350.

Kafka, O.L., Yu, C., Cheng, P., Wolff, S.J., Bennett, J.L., Garboczi, E., Cao, J., Xiao, X., Liu, W.K., 2022. X-ray computed tomography analysis of pore deformation in IN718 made with directed energy deposition via in-situ tensile testing. http://dx.doi.org/10.18434/mds2-2512.

Kim, F.H., Moylan, S.P., Phan, T.Q., Garboczi, E.J., 2020. Investigation of the effect of artificial internal defects on the tensile behavior of laser powder bed fusion 17–4 stainless steel samples: Simultaneous tensile testing and X-Ray computed tomography. Exp. Mech. 60 (7), 987–1004. http://dx.doi.org/10.1007/s11340-020-00604-6.

Krakhmalev, P., Fredriksson, G., Yadroitsava, I., Kazantseva, N., du Plessis, A., Yadroitsev, I., 2016. Deformation behavior and microstructure of Ti6Al4V manufactured by SLM. Phys. Procedia 83, 778–788. http://dx.doi.org/10.1016/j.phpro.2016.08.080, Laser Assisted Net Shape Engineering 9 International Conference on Photonic Technologies Proceedings of the LANE 2016 September 19-22, 2016 Fürth, Germany.

Kruth, J.-P., Vandenbroucke, B., Van Vaerenbergh, J., Naert, I., 2005. Rapid manufacturing of dental prostheses by means of selective laser sintering/melting. In: Proc. AFPR S, Vol. 4. pp. 176–186.

Lambarri, J., Leunda, J., Navas, V.G., Soriano, C., Sanz, C., 2013. Microstructural and tensile characterization of Inconel 718 laser coatings for aeronautic components. Opt. Lasers Eng. 51 (7), 813–821. http://dx.doi.org/10.1016/j.optlaseng.2013.01.011.

Landron, C., Maire, E., Bouaziz, O., Adrien, J., Lecarme, L., Bareggi, A., 2011. Validation of void growth models using X-ray microtomography characterization of damage in dual phase steels. Acta Mater. 59 (20), 7564–7573. http://dx.doi.org/10.1016/j.actamat.2011.08.046.

Lass, E.A., Stoudt, M.R., Williams, M.E., Katz, M.B., Levine, L.E., Phan, T.Q., Gnaeupel-Herold, T.H., Ng, D.S., 2017. Formation of the Ni 3 Nb δ-phase in stress-relieved Inconel 625 produced via laser powder-bed fusion additive manufacturing. Metall. Mater. Trans. A 48 (11), 5547–5558. http://dx.doi.org/10.1007/s11661-017-4304-6.

Lecarme, L., Maire, E., Kumar, A., De Vleeschouwer, C., Jacques, L., Simar, A., Pardoen, T., 2014. Heterogenous void growth revealed by in situ 3-D X-ray microtomography using automatic cavity tracking. Acta Mater. 63, 130–139. http://dx.doi.org/10.1016/j.actamat.2013.10.014.

LePage, W.S., Daly, S.H., Shaw, J.A., 2016. Cross polarization for improved digital image correlation. Exp. Mech. 56 (6), 969–985. http://dx.doi.org/10.1007/s11340-016-0129-2.

Li, Z., Chen, J., Sui, S., Zhong, C., Lu, X., Lin, X., 2020. The microstructure evolution and tensile properties of Inconel 718 fabricated by high-deposition-rate laser directed energy deposition. Addit. Manuf. 31, 100941. http://dx.doi.org/10.1016/j.addma.2019.100941.

Li, X., Liu, Z., Cui, S., Luo, C., Li, C., Zhuang, Z., 2019. Predicting the effective mechanical property of heterogeneous materials by image based modeling and deep learning. Comput. Methods Appl. Mech. Engrg. 347, 735–753. http://dx.doi.org/10.1016/J.CMA.2019.01.005.

Limodin, N., Réthoré, J., Buffière, J.Y., Hild, F., Roux, S., Ludwig, W., Rannou, J., Gravouil, A., 2010. Influence of closure on the 3D propagation of fatigue cracks in a nodular cast iron investigated by X-ray tomography and 3D volume correlation. Acta Mater. 58 (8), 2957–2967. http://dx.doi.org/10.1016/j.actamat.2010.01.024.

Liu, Z., Kafka, O.L., Yu, C., Liu, W.K., 2018. Data-Driven Self-Consistent Clustering Analysis of Heterogeneous Materials with Crystal Plasticity. In: Computational Methods in Applied Sciences, vol. 46, Springer International Publishing, pp. 221–242. http://dx.doi.org/10.1007/978-3-319-60885-3_11.

Liu, F., Lin, X., Huang, C., Song, M., Yang, G., Chen, J., Huang, W., 2011a. The effect of laser scanning path on microstructures and mechanical properties of laser solid formed nickel-base superalloy Inconel 718. J. Alloys Compd. 509 (13), 4505–4509. http://dx.doi.org/10.1016/j.jallcom.2010.11.176.

Liu, F., Lin, X., Yang, G., Song, M., Chen, J., Huang, W., 2011b. Recrystallization and its influence on microstructures and mechanical properties of laser solid formed nickel base superalloy Inconel 718. Rare Metals 30, 433. http://dx.doi.org/10.1007/s12598-011-0319-0.

Maire, E., Bouaziz, O., Di Michiel, M., Verdu, C., 2008. Initiation and growth of damage in a dual-phase steel observed by X-ray microtomography. Acta Mater. 56 (18), 4954–4964. http://dx.doi.org/10.1016/j.actamat.2008.06.015.

Maire, E., Carmona, V., Courbon, J., Ludwig, W., 2007. Fast X-ray tomography and acoustic emission study of damage in metals during continuous tensile tests. Acta Mater. 55 (20), 6806–6815. http://dx.doi.org/10.1016/j.actamat.2007.08.043.

Markopoulos, A.P., Papazoglou, E.-L., Karmiris-Obratański, P., 2020. Experimental study on the influence of machining conditions on the quality of electrical discharge machined surfaces of aluminum alloy Al5052. Machines 8 (12), 1–12. http://dx.doi.org/10.3390/machines8010012.

McGinty, R.D., 2001. Multiscale Representation of Polycrystalline Inelasticity (Ph.D. thesis). Georgia Tech, pp. 1–449.

Nguyen, T.T., Yvonnet, J., Bornert, M., Chateau, C., 2016. Initiation and propagation of complex 3D networks of cracks in heterogeneous quasi-brittle materials: Direct comparison between in situ testing-microct experiments and phase field simulations. J. Mech. Phys. Solids 95, 320–350. http://dx.doi.org/10.1016/j.jmps.2016.06.004.

Ning, F., Hu, Y., Liu, Z., Wang, X., Li, Y., Cong, W., 2018. Ultrasonic vibration-assisted laser engineered net shaping of Inconel 718 parts: Microstructural and mechanical characterization. J. Manuf. Sci. Eng. 140 (6), http://dx.doi.org/10.1115/1.4039441, 061012.

Parimi, L.L., Attallah, M.M., Gebelin, J., Reed, R.C., 2012. Direct laser fabrication of Inconel-718: Effects on distortion and microstructure. In: Superalloys 2012. John Wiley and Sons, Ltd, pp. 509–519. http://dx.doi.org/10.1002/9781118516430.ch56.

Patterson, B.M., Cordes, N.L., Henderson, K., Xiao, X., Chawla, N., 2018. In situ imaging of materials using X-ray tomography. Microsc. Microanal. 24 (S1), 1002–1003. http://dx.doi.org/10.1017/S1431927618005500.

Qi, H., Azer, M., Ritter, A., 2009. Studies of standard heat treatment effects on microstructure and mechanical properties of laser net shape manufactured INCONEL 718. Metall. Mat. Trans. A 40, 2410–2422. http://dx.doi.org/10.1007/s11661-009-9949-3.

Samei, J., Amirmaleki, M., Ventura, A.P., Pawlikowski, G.T., Bayes, M., Misiolek, W.Z., Wilkinson, D.S., 2020. In-situ X-ray tomography analysis of the evolution of pores during deformation of a Cu-Sn alloy fabricated by selective laser melting. Addit. Manuf. 34, 101196. http://dx.doi.org/10.1016/j.addma.2020.101196.

Schneider, J., 2020. Comparison of microstructural response to heat treatment of Inconel 718 prepared by three different metal additive manufacturing processes. JOM 72 (3), 1085–1091. http://dx.doi.org/10.1007/s11837-020-04021-x.

Shamsaei, N., Yadollahi, A., Bian, L., Thompson, S.M., 2015. An overview of direct laser deposition for additive manufacturing; part II: Mechanical behavior, process parameter optimization and control. Addit. Manuf. 8, 12–35. http://dx.doi.org/10.1016/j.addma.2015.07.002.

Small, K.B., Englehart, D.A., Christman, T.A., 2017. A guide to etching specialty alloys for microstructural evaluation. URL: https://www.carpentertechnology.com/blog/a-guide-to-etching-specialty-alloys.

Sochalski-Kolbus, L.M., Payzant, E.A., Cornwell, P.A., Watkins, T.R., Babu, S.S., Dehoff, R.R., Lorenz, M., Ovchinnikova, O., Duty, C., 2015. Comparison of residual stresses in Inconel 718 simple parts made by electron beam melting and direct laser metal sintering. Metall. Mater. Trans. A 46 (3), 1419–1432. http://dx.doi.org/10.1007/s11661-014-2722-2.

Solutions, C., 2018. VIC-2D Version 6, Correlated Solutions, Irmo SC. https://www.correlatedsolutions.com/vic-2d/.

Steuwer, A., Daniels, J.E., 2011. In-situ stress and strain measurements around cracks using synchrotron X-ray diffraction. J. Strain Anal. Eng. Des. 46 (7), 593–606. http://dx.doi.org/10.1177/0309324711408501.

Steuwer, A., Edwards, L., Pratihar, S., Ganguly, S., Peel, M., Fitzpatrick, M.E., Marrow, T.J., Withers, P.J., Sinclair, I., Singh, K.D., Gao, N., Buslaps, T., Buffière, J.Y., 2006. In situ analysis of cracks in structural materials using synchrotron X-ray tomography and diffraction. Nucl. Instrum. Methods Phys. Res. 246 (1), 217–225. http://dx.doi.org/10.1016/j.nimb.2005.12.063.

Sui, S., Tan, H., Chen, J., Zhong, C., Li, Z., Fan, W., Gasser, A., Huang, W., 2019. The influence of laves phases on the room temperature tensile properties of Inconel 718 fabricated by powder feeding laser additive manufacturing. Acta Mater. 164, 413–427. http://dx.doi.org/10.1016/j.actamat.2018.10.032.

Toda, H., Maire, E., Aoki, Y., Kobayashi, M., 2011. Three-dimensional strain mapping using in situ X-ray synchrotron microtomography. J. Strain Anal. Eng. Des. 46 (7), 549–561. http://dx.doi.org/10.1177/0309324711408975.

Voisin, T., Calta, N.P., Khairallah, S.A., Forien, J.-B., Balogh, L., Cunningham, R.W., Rollett, A.D., Wang, Y.M., 2018. Defects-dictated tensile properties of selective laser melted Ti-6Al-4V. Mater. Des. 158, 113–126. http://dx.doi.org/10.1016/j.matdes.2018.08.004.

Watring, D.S., Benzing, J.T., Kafka, O.L., Liew, L.A., Moser, N.H., Erickson, J., Hrabe, N., Spear, A.D., 2022. Evaluation of a modified void descriptor function to uniquely characterize pore networks and predict fracture-related properties in additively manufactured metals. Acta Mater. 223, 117464. http://dx.doi.org/10.1016/j.actamat.2021.117464.

Weck, A., Wilkinson, D., Maire, E., Toda, H., 2008. Visualization by X-ray tomography of void growth and coalescence leading to fracture in model materials. Acta Mater. 56 (12), 2919–2928. http://dx.doi.org/10.1016/j.actamat.2008.02.027.

Wejdemann, C., Lienert, U., Pantleon, W., 2010. In situ measurements of X-ray peak profile asymmetry from individual grains. J. Phys.: Conf. Ser. 240, 012160. http://dx.doi.org/10.1088/1742-6596/240/1/012160.

Wolff, S.J., Gan, Z., Lin, S., Bennett, J.L., Yan, W., Hyatt, G., Ehmann, K.F., Wagner, G.J., Liu, W.K., Cao, J., 2019. Experimentally validated predictions of thermal history and microhardness in laser-deposited Inconel 718 on carbon steel. Addit. Manuf. 27, 540–551. http://dx.doi.org/10.1016/j.addma.2019.03.019.

Xavier, M.S., Yang, S., Comte, C., Bab-Hadiashar, A., Wilson, N., Cole, I., 2020. Nondestructive quantitative characterisation of material phases in metal additive manufacturing using multi-energy synchrotron X-rays microtomography. Int. J. Adv. Manuf. Technol. 106 (5), 1601–1615. http://dx.doi.org/10.1007/s00170-019-04597-y.

Yan, W., Lian, Y., Yu, C., Kafka, O.L., Liu, Z., Liu, W.K., Wagner, G.J., 2018. An integrated process–structure–property modeling framework for additive manufacturing. Comput. Methods Appl. Mech. Engrg. 339, 184–204. http://dx.doi.org/10.1016/j.cma.2018.05.004.

Yu, C., 2019. Multiscale Clustering Analysis (Ph.D. thesis). Northwestern University.

Yu, C., Kafka, O.L., Liu, W.K., 2019. Self-consistent clustering analysis for multiscale modeling at finite strains. Comput. Methods Appl. Mech. Engrg. 349, 339–359. http://dx.doi.org/10.1016/j.cma.2019.02.027.

Yuan, K., Guo, W., Li, P., Wang, J., Su, Y., Lin, X., Li, Y., 2018. Influence of process parameters and heat treatments on the microstructures and dynamic mechanical behaviors of Inconel 718 superalloy manufactured by laser metal deposition. Mater Sci. Eng. A 721, 215–225. http://dx.doi.org/10.1016/j.msea.2018.02.014.

Yvell, K., Grehk, T.M., Hedström, P., Borgenstam, A., Engberg, G., 2018. Microstructure development in a high-nickel austenitic stainless steel using EBSD during in situ tensile deformation. Mater. Charact. 135, 228–237. http://dx.doi.org/10.1016/j.matchar.2017.11.046.

Zhai, Y., Lados, D.A., Brown, E.J., Vigilante, G.N., 2019. Understanding the microstructure and mechanical properties of Ti-6Al-4V and Inconel 718 alloys manufactured by laser engineered net shaping. Addit. Manuf. 27, 334–344. http://dx.doi.org/10.1016/j.addma.2019.02.017.

Zhang, Y., Yang, L., Lu, W., Wei, D., Meng, T., Gao, S., 2020. Microstructure and elevated temperature mechanical properties of IN718 alloy fabricated by laser metal deposition. Mater. Sci. Eng. A 771, 138580. http://dx.doi.org/10.1016/j.msea.2019.138580.

Zhao, X., Chen, J., Lin, X., Huang, W., 2008. Study on microstructure and mechanical properties of laser rapid forming Inconel 718. Mater. Sci. Eng. A 478 (1), 119–124. http://dx.doi.org/10.1016/j.msea.2007.05.079.

Zhong, C., Gasser, A., Kittel, J., Wissenbach, K., Poprawe, R., 2016. Improvement of material performance of Inconel 718 formed by high deposition-rate laser metal deposition. Mater. Des. 98, 128–134. http://dx.doi.org/10.1016/j.matdes.2016.03.006.